Mechanisms of Asymmetric Membrane Formation in Nonsolvent-Induced Phase Separation

Jan Ulric Garcia,[†,‡] Tatsuhiro Iwama,[¶] Eva Y. Chan,[†] Douglas R. Tree,[§] Kris T. Delaney,[‡] and Glenn H. Fredrickson[*,†,‡,‖]

[†]*Dept. of Chemical Engineering, University of California, Santa Barbara, CA 93106, USA*

[‡]*Materials Research Laboratory, University of California, Santa Barbara, CA 93106, USA*

[¶]*Asahi Kasei Corporation, 2-1 Samejima, Fuji, Shizuoka 416-8501, Japan*

[§]*Dept. of Chemical Engineering, Brigham Young University, Provo, UT 84602, USA*

[‖]*Dept. of Materials, University of California, Santa Barbara, CA 93106, USA*

E-mail: ghf@ucsb.edu

Abstract

We report the first simulations of nonsolvent-induced phase separation (NIPS) that predict membrane microstructures with graded asymmetric pore size distribution. In NIPS, a polymer solution film is immersed in a nonsolvent bath, enriching the film in nonsolvent, and leading to phase separation that forms a solid polymer-rich membrane matrix and polymer-poor membrane pores. We demonstrate how mass-transfer-induced spinodal decomposition, thermal fluctuations, and glass-transition dynamics—implemented with mobility contrast between the polymer-rich and polymer-poor phases—are essential to the formation of asymmetric membrane microstructures. Specifically, we show that the competition between the propagation of the phase-separation and glass-transition fronts determines the degree of pore-size asymmetry.

We also explore the sensitivity of these microstructures to the initial film composition, and compare their formation in 2D and 3D.

Polymer membranes are essential to water security: they purify our drinking water, desalinate sea water into potable water, and treat wastewater before its release to the environment.[1,2] The separation performance of these membranes is largely determined by their microstructure. An asymmetric microstructure is advantageous for many applications:[3] the smaller pores on the feed-side of the membrane enable separation, while larger pores deeper into the membrane provide mechanical support with minimal resistance to permeate flow. Nonsolvent-induced phase separation (NIPS)[4,5]—also known as "wet-phase inversion" or the "Loeb-Sourirajan process"[6]—is a typical way to make asymmetric membranes. In NIPS, a homogeneous polymer solution is cast into a film and then immersed in a nonsolvent bath. The exchange of nonsolvent and solvent between the bath and the film enriches the film in nonsolvent, inducing phase separation of the film to a polymer-rich phase that becomes the membrane matrix and a polymer-poor phase that becomes the membrane pores.

Selecting process parameters to target specific membrane microstructures is challenging due to our limited understanding of NIPS; membrane manufacturers rely on heuristics, but this approach limits the development of more effective membranes. To understand NIPS, several research groups have modeled the NIPS system with Flory-Huggins thermodynamics coupled to multicomponent transport equations. Numerical techniques used to simulate NIPS include lattice Boltzmann,[7] smoothed particle hydrodynamics,[8] and phase-field simulations.[9–12] While these studies have shown mass-transfer-induced phase separation, they predicted either the unrealistic formation of alternating polymer-rich and polymer-poor layers aligned with the film-bath interface, or the formation of microstructures with homogeneous pore size distributions. To our knowledge, no existing numerical study of NIPS has shown the formation of graded asymmetric pore size distributions, suggesting that physics essential to NIPS membrane formation is missing in the existing models. In their numerical study of membrane formation by thermally-induced phase separation (TIPS), Millett and co-

workers[13] demonstrated the formation of graded asymmetric microstructures by anisotropic cooling of a homogeneous film into a phase-separated membrane. Based on their TIPS model and the NIPS studies mentioned above, we hypothesize that in addition to mass-transfer-induced phase separation, two more mechanisms are essential to the formation of asymmetric microstructures: thermal fluctuations and structural arrest due to solidification of the polymer-rich phase. Solidification mechanisms[14] in NIPS include crystallization, gelation, and vitrification; we select glassy dynamics for the solidification mechanism in this study.

We have modified our phase-field model from previous NIPS studies[10–12] to incorporate thermal fluctuations and a glass transition. To focus on these two features, we exclude hydrodynamics in this study and use a system of diffusion equations to model NIPS. Hydrodynamics are discussed further in the Supporting Information. Using R_0, the root-mean-square (RMS) end-to-end distance of a reference polymer with degree of polymerization N_r as the characteristic length scale, τ, the Rouse time of the reference polymer in a solvent of viscosity, η_s, as the characteristic time scale, and $N_r k_B T/b^3$ as the characteristic chemical potential scale, we present our model in dimensionless form:

$$\frac{\partial \phi_i(\boldsymbol{r},t)}{\partial t} = \boldsymbol{\nabla}\cdot\left[\sum_j^{p,n} M_{ij}(\{\phi_i\})\boldsymbol{\nabla}\mu_j(\{\phi_i\})\right] + \alpha N_r^{-1/4}\theta_i(\boldsymbol{r},t) \tag{1}$$

where $\phi_p(\boldsymbol{r},t)$ and $\phi_n(\boldsymbol{r},t)$ are the polymer and nonsolvent volume fractions, M_{ij} is the mobility matrix, μ_j is the chemical potential of species j, and $\theta_i(\boldsymbol{r},t)$ are noise terms that follow fluctuation-dissipation theorem (FDT) statistics,[15]

$$\langle \theta_i(\boldsymbol{r},t)\rangle = 0 \tag{2a}$$

$$\langle \theta_i(\boldsymbol{r},t)\theta_j(\boldsymbol{r'},t')\rangle = -2\boldsymbol{\nabla}\cdot[M_{ij}(\{\phi_i\})\boldsymbol{\nabla}\delta(\boldsymbol{r}-\boldsymbol{r'})]\delta(t-t'). \tag{2b}$$

The incompressibility assumption implicitly gives the solvent volume fraction, $\phi_s = 1-\phi_p-\phi_n$. The noise-scaling factor, $\alpha \in [0,1]$, reduces the strength of the fluctuations in Eq 1

for numerical stability, where $\alpha = 0$ makes the dynamics purely deterministic while $\alpha = 1$ sets noise strengths consistent with FDT. For all stochastic simulations in this work, we set $\alpha = 0.04$; although this value breaks consistency with FDT, we show that $\alpha = 0.04$ is large enough to eliminate nonphysical membrane features observed in purely deterministic simulations. A glass transition is introduced in the model through the use of concentration-dependent mobilities,

$$M_{pp} = \phi_p(1 - \phi_p)/\eta \tag{3a}$$

$$M_{pn} = M_{np} = -\phi_p\phi_n/\eta \tag{3b}$$

$$M_{nn} = \phi_n(1 - \phi_n)/\eta, \tag{3c}$$

where η is the concentration-dependent local viscosity. We confer glassy dynamics by modeling η as a sigmoidal function of the local polymer volume fraction, $\phi_p(\boldsymbol{r})$:

$$\eta = 1 + \frac{\eta_p/\eta_s - 1}{1 + \exp\left(-\frac{1}{w}\left(\phi_p(\boldsymbol{r}) - \phi_p^*\right)\right)} \tag{4}$$

where η_p/η_s represents the pure-component viscosity ratio of the polymer and the solvent (implicitly assuming $\eta_n = \eta_s$), w controls the width of the sigmoid, and ϕ_p^* represents the glass-transition concentration. A sigmoid mimics the Vogel-Fulcher-Tamman-Hesse (VFTH) and Williams-Landel-Ferry (WLF) equations[16] with the exponential growth of viscosity, while bounding its maximum value for computational stability. Setting $w = 5 \times 10^{-3}$ approximates η as a step function, narrow enough such that $\eta = 1$ at $\phi_p = 0$, but wide enough to avoid computational issues associated with a mathematical discontinuity. This choice implies that for ϕ_p values far enough from ϕ_p^*, $\eta = 1$ for $\phi_p(\boldsymbol{r}) < \phi_p^*$, while $\eta = \eta_p/\eta_s$ for $\phi_p(\boldsymbol{r}) > \phi_p^*$. Thus, local mobilities are unscaled in non-glassy regions but they are scaled by η_p/η_s in glassy regions. Setting $\eta_p/\eta_s = 1$ disables the glass transition while $\eta_p/\eta_s = 1 \times 10^4$ enables it. The latter value serves as a balance between faithfully representing a physical glass transition and accessing practical simulation times; we further justify this choice in the

Supporting Information.

Finally, the chemical potential terms in Eq. 1 are calculated as the functional derivatives of the system free energy, $\mu_i = \delta F/\delta\phi_i$, where Flory-Huggins-de Gennes thermodynamics describe the free energy:

$$F\left[\{\phi_i\}\right] = \int \mathrm{d}\mathbf{r}\left[f(\{\phi_i\}) + g(\{\phi_i\})\right] \tag{5a}$$

$$f(\{\phi_i\}) = \sum_{i}^{p,n,s} \frac{\phi_i}{N_i} \ln \phi_i + \frac{1}{2} \sum_{i \neq j}^{p,n,s} \chi_{ij} \phi_i \phi_j \tag{5b}$$

$$g(\{\phi_i\}) = \frac{1}{2} \begin{bmatrix} \boldsymbol{\nabla}\phi_p & \boldsymbol{\nabla}\phi_n \end{bmatrix} \begin{bmatrix} \kappa_p + \kappa_s & \kappa_s \\ \kappa_s & \kappa_n + \kappa_s \end{bmatrix} \begin{bmatrix} \boldsymbol{\nabla}\phi_p \\ \boldsymbol{\nabla}\phi_n \end{bmatrix}. \tag{5c}$$

Eqs. 5b and 5c represent the bulk and interfacial free energy contributions, respectively. We set the degree of polymerization of each component as, $N_p = 20, N_n = N_s = 1$, with the reference, $N_r = 20$, the interaction parameters as, $\chi_{pn} = 1.048$, $\chi_{ps} = \chi_{ns} = 0$, and the square-gradient coefficients as, $\kappa_p = \kappa_n = \kappa_s = 1.5$. We provide further details of our model and numerical methods in the Supporting Information.

Figure 1 shows the ternary phase diagram for the NIPS system in this work. We set initial film compositions near the critical point based on our findings that such compositions are necessary for mass-transfer-induced phase separation.[12] The nonsolvent bath composition was set to nearly pure nonsolvent, leaving only small amounts of polymer and solvent to avoid the singular composition bounds of the Flory-Huggins functional. We initialized the top-half of the simulation box as the bath and the bottom-half as the homogeneous film. No-flux boundary conditions were implemented at the bottom of the film and at the top of the bath, while periodic boundary conditions were imposed on the lateral sides of the simulation box. To visualize results, only domains corresponding to the initial homogeneous film were shown, omitting the nonsolvent bath for clarity. The glass-transition concentration was set to $\phi_p^* = 0.33$, a value close enough to the initial film compositions so that mobility contrast effects manifest soon after phase separation. In reality, ϕ_p^* is not arbitrary as it

changes with dope formulation and temperature.[17,18] We leave the effects of varying ϕ_p^* to future work.

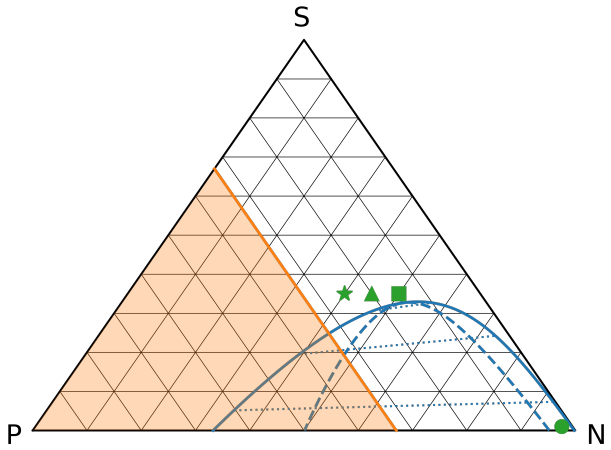

Figure 1: Ternary phase diagram for our NIPS system. Each vertex corresponds to pure polymer (P), pure solvent (S), and pure nonsolvent (N) compositions. The solid blue line marks the binodal while the dashed blue line marks the spinodal, as calculated with Flory-Huggins thermodynamics where $\chi_{pn} = 1.048$, $\chi_{ps} = \chi_{ns} = 0$, $N_p = 20$, $N_n = N_s = 1$. The dotted blue lines are examples of tie lines. The solid orange line marks the glass transition concentration, $\phi_p^* = 0.33$. Any composition within the shaded orange area is considered "glassy." The green circle marks the bath composition, which is almost pure nonsolvent ($\phi_p = 0.02, \phi_n = 0.97$). The green star ($\phi_p = 0.25, \phi_n = 0.40$), green triangle ($\phi_p = 0.20, \phi_n = 0.45$), and green square ($\phi_p = 0.15, \phi_n = 0.50$) mark the initial homogeneous film compositions used in this study.

Figure 2 illustrates the effects of thermal fluctuations on mass-transfer-driven microstructure evolution. In the absence of fluctuations (Figure 2a), a pattern of alternating polymer-rich and polymer-poor layers forms parallel to the film-bath interface, consistent with other numerical studies of NIPS.[8,12] We attribute the propagation of the ordered pattern to surface-directed spinodal decomposition (SDSD).[19] In contrast, enabling fluctuations (Figure 2b) introduces disorder to the dynamics, disrupting the propagation of this ordered pattern with more isotropic bulk spinodal decomposition. The two rows of polymer-poor circles at $t = 1 \times 10^3$, manifest the competition between the order imposed by SDSD and the disorder due to thermal fluctuations. Morphologies at later times show that deeper into the film, the influence of SDSD wanes and bulk spinodal decomposition dominates. As shown, setting

$\alpha = 0.04$ is enough to break the ordered pattern, but the effects of stronger fluctuations, including phase separation by nucleation, remain unexplored; we leave this complexity to future work.

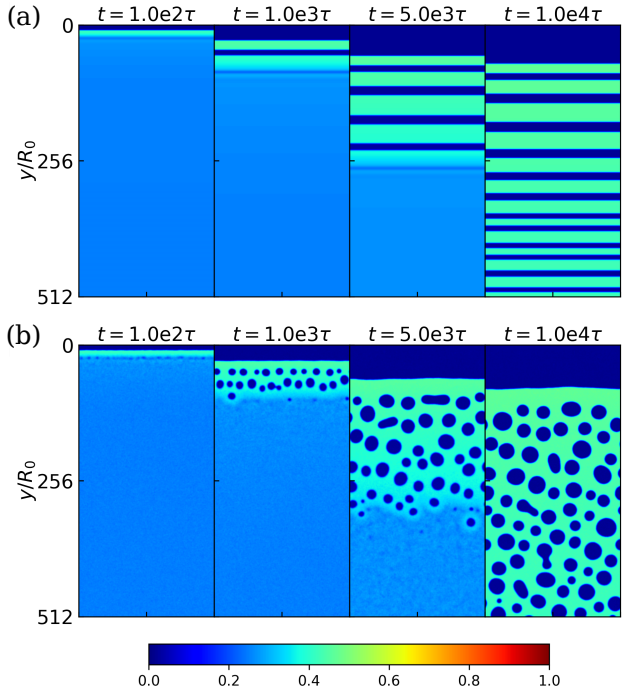

Figure 2: NIPS simulations (a) without ($\alpha = 0$) and (b) with ($\alpha = 0.04$) thermal fluctuations. Each box shown is $256R_0 \times 512R_0$. The y-coordinate corresponds to film depth, where $y = 0$ is the film-bath interface and $y = 512$ is the bottom of the film. The bath is not visualized for clarity. Polymer-rich regions are light green and polymer-poor regions are dark blue, color bar included for ϕ_p. Initial film composition is $(\phi_p = 0.25, \phi_n = 0.40)$, corresponding to the green star in Figure 1. No glass transition effects are introduced, *i.e.*, $\eta_p/\eta_s = 1$ for both (a) and (b).

Figure 3 shows the effects of the glass transition on the 2D microstructure. In the absence of a glass transition (Figure 3a), the progress of microstructure formation varies with film depth at early times (first three frames). A phase-separation front due to SDSD follows nonsolvent diffusion into the film. Just above the phase-separation front, domain sizes increase towards the film-bath interface; but far enough from the front, domain sizes become more homogeneous, a profile that eventually manifests through the whole film at late times (last two frames). We attribute these observations to domain coarsening. In a bulk quench of a system that coarsens only by diffusion, the characteristic domain size, L, follows

the Lifshitz-Slyozov-Wagner[20,21] scaling law, $L \sim t^{1/3}$. Assuming that a similar power law applies to mass-transfer-induced phase separation, *i.e.,* the coarsening mechanisms involved do not change the exponent, we posit that for phase-separated domains,

$$L(t, y) \sim (t - t_p(y))^{1/3}, \tag{6}$$

where $t_p(y)$ is the time when the phase-separation front arrived at film depth, y. Eq 6 offers a crude rationalization for our simulations since phase-separated domains in 2D span several values of y; nevertheless, it proves useful for the discussion. For domains just above the phase-separation front, the quantity $(t - t_p(y))$ increases away from the front, consistent with the observed domain-size profile. However, for domains far enough from the phase-separation front, we can approximate $(t - t_p(y)) \approx t$, implying L is no longer a function of film depth for these mature domains. The same approximation applies to all values of y, long after the phase separation front has reached the bottom of the film, explaining the symmetric pore-size distribution at late times. We discuss the computation of the average domain size for each y-slice in the Supporting Information.

In contrast, the glass transition dramatically changes the microstructure (Figure 3b). To begin, a polymer-rich skin forms at the film-bath interface. Thermal fluctuations introduce perforations on the polymer-rich skin before it turns glassy. Due to the imposed mobility contrast, the glassy skin then acts as a barrier to nonsolvent entry, only allowing the nonsolvent to penetrate the film through the perforations, consistent with the proposed mechanism by Smolders and co-workers.[22–24] The perforations grow deeper into the film, forming finger-like structures that eventually become a network of pores—a stark contrast from the closed-pore morphology formed without the glass transition. Though similar in appearance, these "finger-like structures" are distinct from macrovoids[25,26] that span the thickness of a membrane; we make no claims about macrovoid formation in this work.

In addition to the qualitative change in morphology, the glass transition also leads to a

positive pore-size gradient from the film-bath interface to the glass-transition front, evidenced by the positive slope of the film-depth vs. domain-size curve from $y = 0$ to the orange glass-transition line. *The mechanism responsible for this pore-size gradient is the increasing lead of the phase-separation front over the glass-transition front.* We plot the propagation dynamics of these two fronts in the Supporting Information. Domain features above the glass-transition front are frozen while those below it are free to evolve. Following the same assumptions made for Eq 6, we posit that for domains above the glass-transition front:

$$L(y) \sim (t_g(y) - t_p(y))^{1/3}, \tag{7}$$

where $t_g(y)$ and $t_p(y)$ are the times when the glass-transition and phase-separation fronts arrived at film depth, y, respectively. Again, Eq 7 offers a crude rationalization for our simulations, but it proves useful for the discussion. Since the phase-separation front moves faster than the glass-transition front, the quantity $(t_g(y) - t_p(y))$ increases with film depth, leading to the asymmetric pore-size distribution. This proposed mechanism is not unfounded; using in-situ experiments, McHugh and co-workers[27] correlated the transition from a macrovoid morphology to a sponge microstructure with changes to the propagation dynamics of these two fronts, demonstrating their importance to shaping membrane morphology.

While Figure 3 shows microstructures with a continuous polymer-rich phase, Figure 4 demonstrates that less polymer content in the initial film can lead to an inversion of the continuous phase to polymer-poor. In the absence of a glass transition (Figure 3a vs. Figure 4a), the inversion itself does not change the propagation kinetics of the phase-separation front; the front in Figure 4a has a slight lead in penetrating the film only because its initial film composition is closer to the binodal, allowing nonsolvent entry to induce phase separation earlier. On the other hand, the inversion alters front-propagation dynamics in the presence of a glass transition (Figure 3b vs. Figure 4b). Since the polymer-poor phase is continuous in Figure 4b, nonsolvent can penetrate the film without having to form finger-like

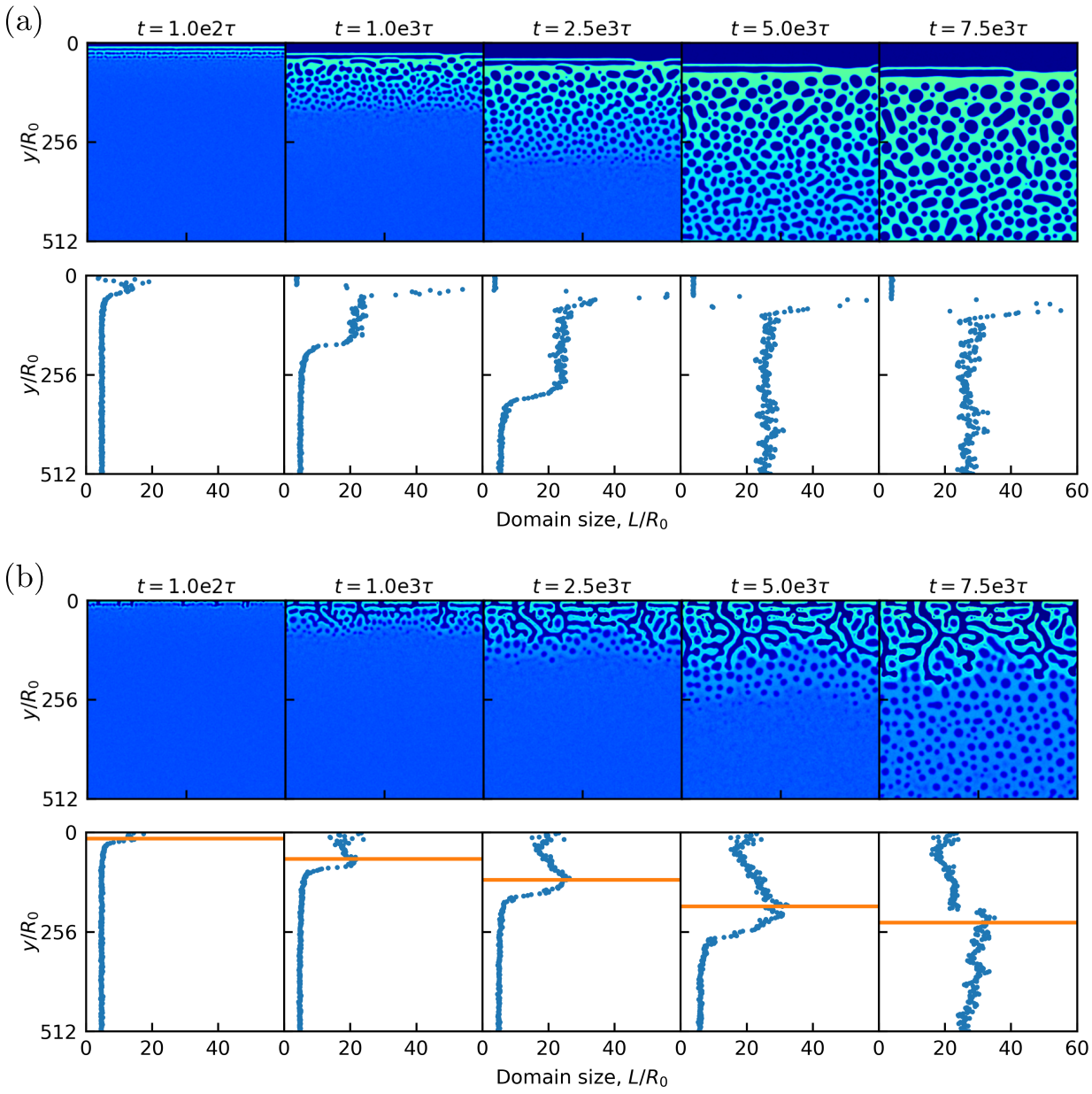

Figure 3: NIPS simulations in 2D and their domain size profiles (a) without and (b) with glass transition effects for the initial film composition of $(\phi_p = 0.20, \phi_n = 0.45)$, corresponding to the green triangle in Figure 1. Mobility contrasts set at (a) $\eta_p/\eta_s = 1$, (b) $\eta_p/\eta_s = 10^4$. Each density plot shown is $512R_0 \times 512R_0$. The y-coordinate corresponds to film depth, where $y = 0$ is the film-bath interface and $y = 512$ is the bottom of the film. The bath is not visualized for clarity. Polymer-rich regions are light green and polymer-poor regions are dark blue, ϕ_p color bar included in Figure 2. The orange line (glass-transition front) in the domain size profile for (b) corresponds to the deepest point in the film where at least one grid point has crossed the glass transition concentration, ϕ_p^*.

structures, allowing both the phase-separation and glass-transition fronts to propagate more quickly. However, this speed-up unevenly favors the glass-transition front, effectively reducing $(t_g(y) - t_p(y))$ for frozen domains. As a consequence, the domain-size gradient from the film-bath interface to the glass-transition front becomes less pronounced in Figure 4b than it was for Figure 3b.

The dynamics of membrane formation also change in 3D, owing to the greater tendency of domains to stay continuous after phase separation. Figure 5 shows the 3D equivalent of Figure 3b. The finger-like structures in 2D translate to a 3D pore network that allows the nonsolvent to penetrate the film faster in 3D. The bicontinuous microstructure in 3D leads to speed-ups for both the phase-separation and glass-transition fronts. Again, the speed-up unevenly favors the latter—especially for deeper points in the film—leading to a less-pronounced gradient in domain size for the 3D microstructure.

Similar effects of bicontinuity are shown in Figure 6, the 3D equivalent of Figure 4b. The discrete polymer-rich phase in the 2D morphology translates to a mostly continuous structure in 3D. Despite the continuous polymer-rich phase, the higher dimensionality still leads to speed-ups for both the phase-separation and glass-transition fronts. The domain-size gradient in 3D is again less-pronounced due to the larger speed-up of the glass-transition front.

Despite the bicontinuity of both 3D morphologies (Figure 5 vs. Figure 6), initial film composition remains important to the propagation of the phase-separation and glass-transition fronts. Less polymer content in the initial film leads to less resistance to mass-transfer, evidenced by faster propagation of both fronts in Figure 6. However, the faster advance of both fronts also leads to less pronounced domain-size asymmetry, as demonstrated by the decreased slope in the film-depth vs. domain-size curve in Figure 6.

While the asymmetric structures observed here in both 2D and 3D are in qualitative agreement with experiments,[28,29] we do not attempt quantitative comparisons. Instead, our focus was on gaining a mechanistic understanding of NIPS by building a model step-

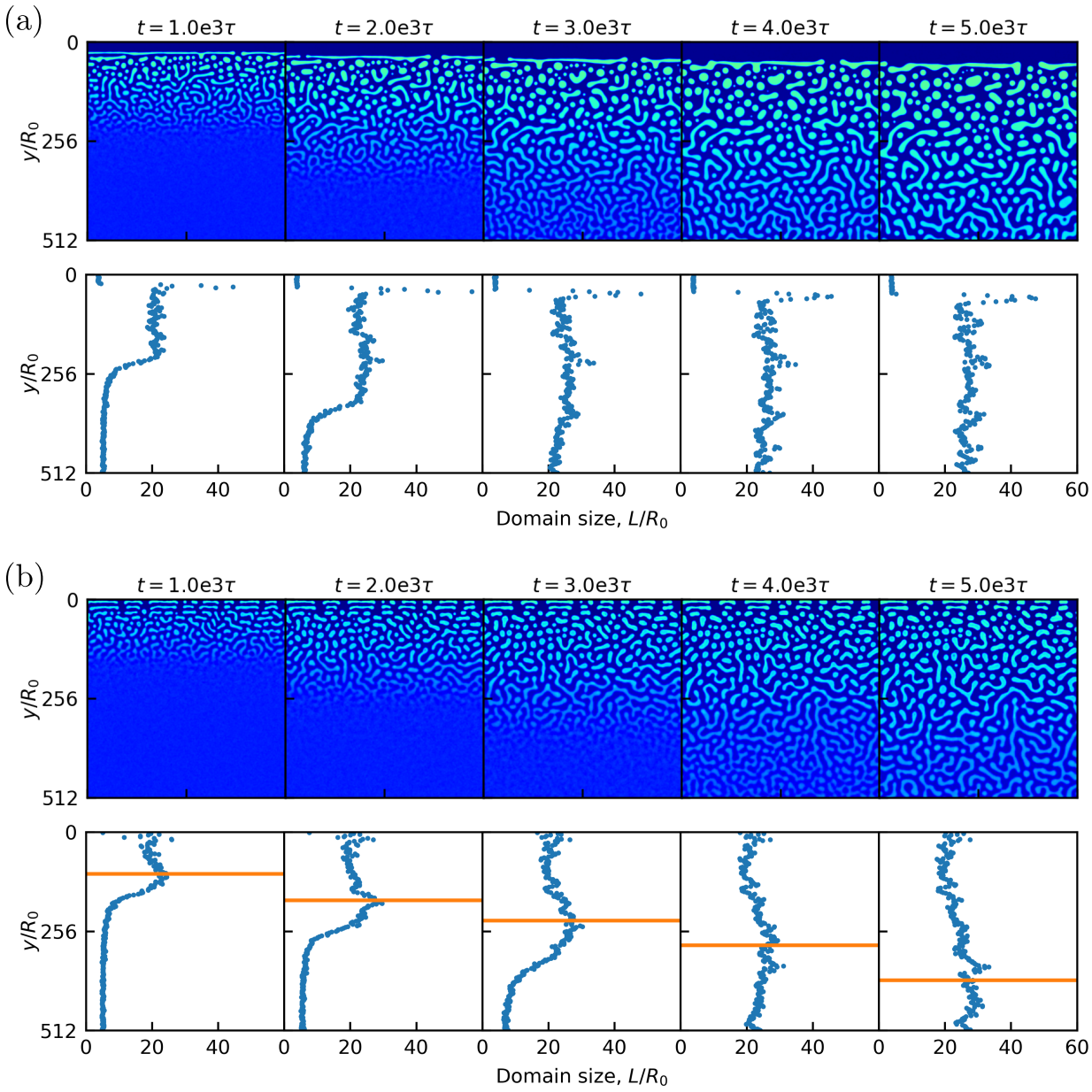

Figure 4: NIPS simulations in 2D and their domain size profiles (a) without and (b) with glass transition effects for the initial film composition of $(\phi_p = 0.15, \phi_n = 0.50)$, corresponding to the green square in Figure 1. Mobility contrasts set at (a) $\eta_p/\eta_s = 1$, (b) $\eta_p/\eta_s = 10^4$. Each density plot shown is $512R_0 \times 512R_0$. The y-coordinate corresponds to film depth, where $y = 0$ is the film-bath interface and $y = 512$ is the bottom of the film. The bath is not visualized for clarity. Polymer-rich regions are light green and polymer-poor regions are dark blue, ϕ_p color bar included in Figure 2. The orange line (glass-transition front) in the domain size profile for (b) corresponds to the deepest point in the film where at least one grid point has crossed the glass transition concentration, ϕ_p^*.

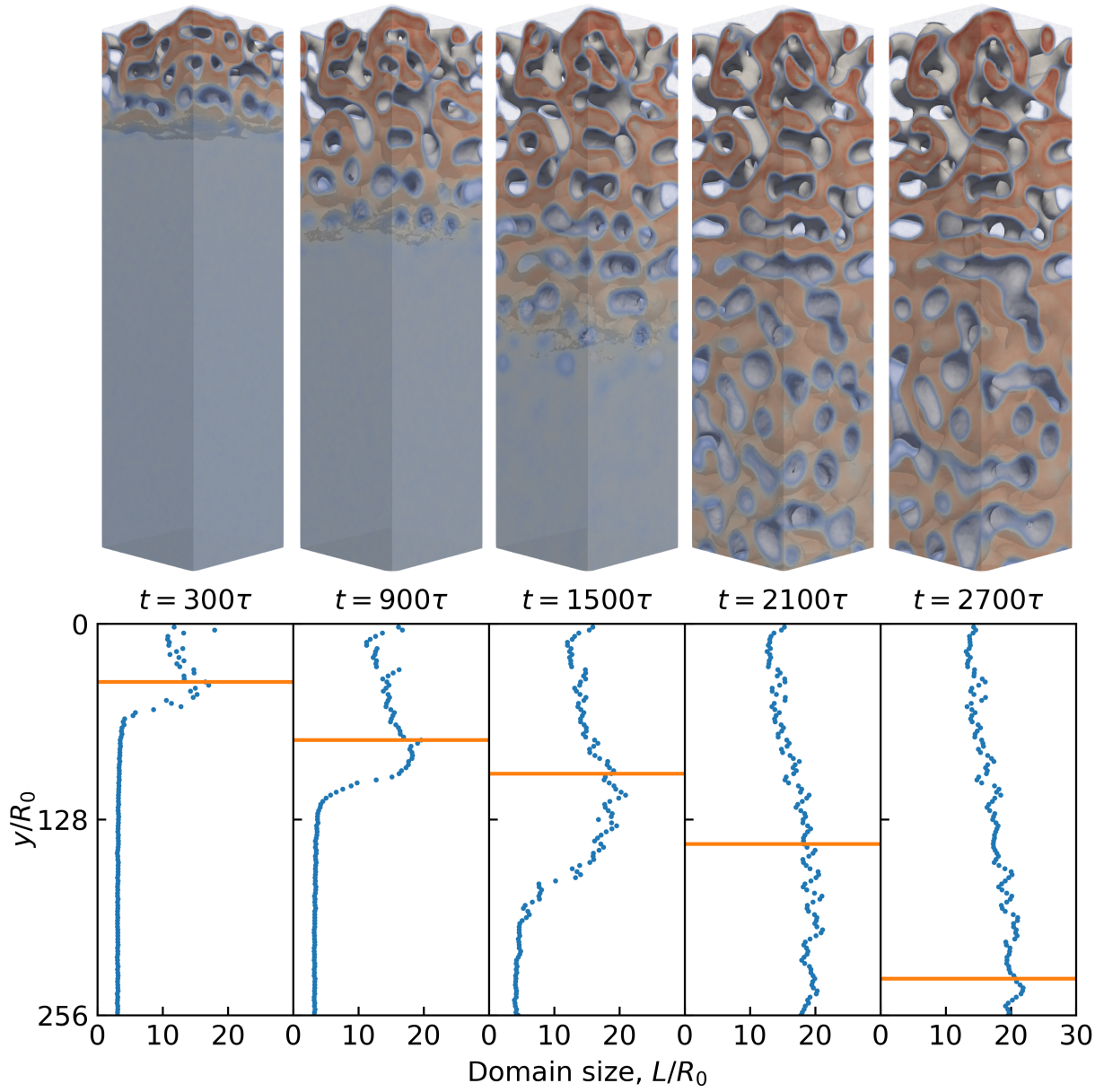

Figure 5: NIPS simulation in 3D and its domain size profile for the initial film composition of $(\phi_p = 0.20, \phi_n = 0.45)$, corresponding to the green triangle in Figure 1. Mobility contrast set at $\eta_p/\eta_s = 10^4$. Each density plot shown is $64R_0 \times 256R_0 \times 64R_0$. The y-coordinate corresponds to film depth, where $y = 0$ is the film-bath interface and $y = 256$ is the bottom of the film. The bath is not visualized for clarity. Polymer-rich regions are opaque red, polymer-poor regions are translucent blue, and the isosurface is opaque beige. The orange line (glass-transition front) in the domain size profile corresponds to the deepest point in the film where at least one grid point has crossed the glass transition concentration, ϕ_p^*.

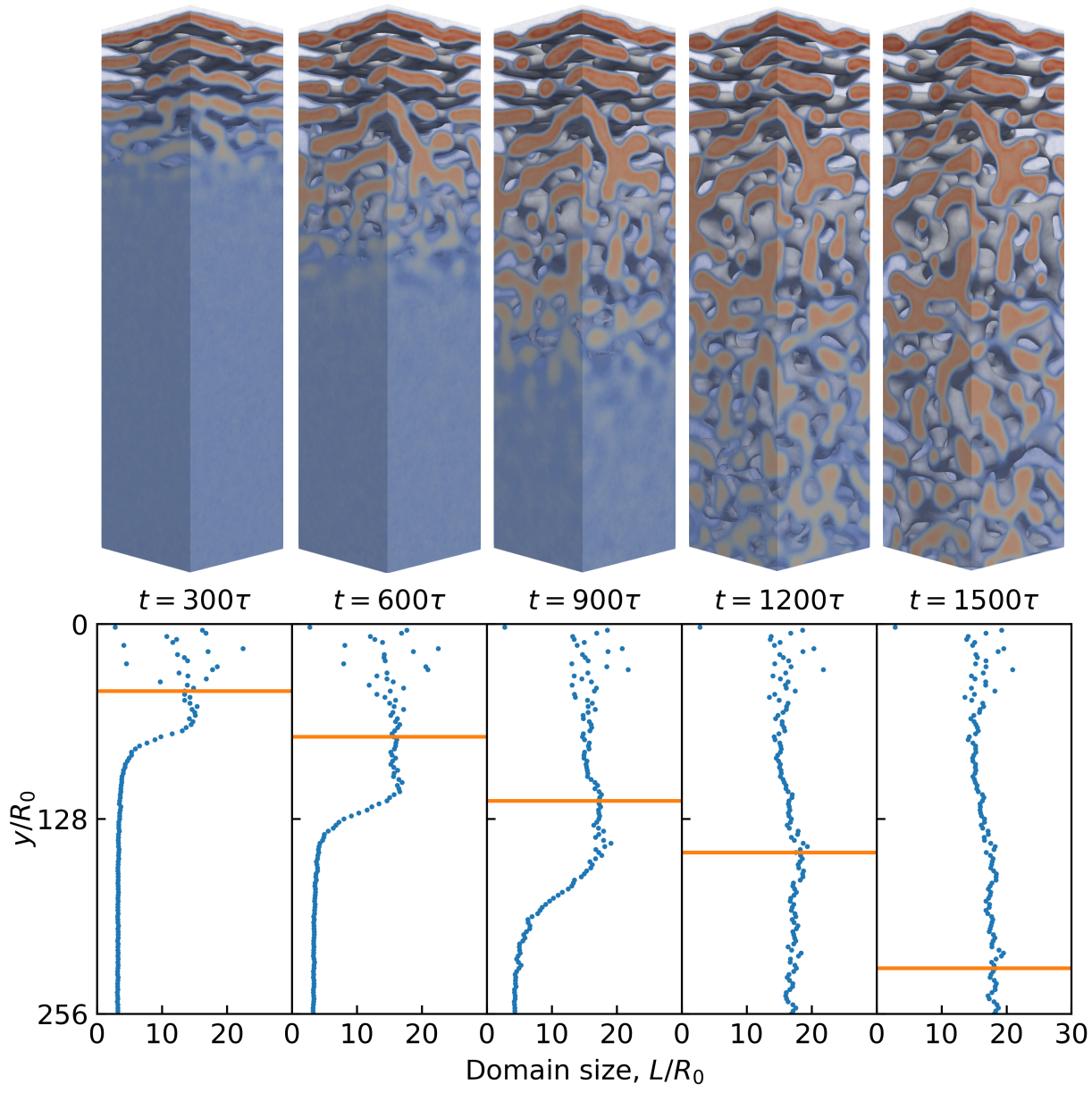

Figure 6: NIPS simulation in 3D and its domain size profile for the initial film composition of $(\phi_p = 0.15, \phi_n = 0.50)$, corresponding to the green square in Figure 1. Mobility contrast set at $\eta_p/\eta_s = 10^4$. Each density plot shown is $64R_0 \times 256R_0 \times 64R_0$. The y-coordinate corresponds to film depth, where $y = 0$ is the film-bath interface and $y = 256$ is the bottom of the film. The bath is not visualized for clarity. Polymer-rich regions are opaque red, polymer-poor regions are translucent blue, and the isosurface is opaque beige. The orange line (glass-transition front) in the domain size profile corresponds to the deepest point in the film where at least one grid point has crossed the glass transition concentration, ϕ_p^*.

by-step, adding complexity in each step and considering its role in membrane formation. We demonstrated that mass-transfer-induced phase separation, thermal fluctuations, and a structural arrest mechanism are necessary and sufficient to form graded asymmetric pore-size distributions. However, other complexities in experiments remain unexplored, notably hydrodynamics. As velocities are scaled by the inverse of mixture viscosity, we assume that flows in any continuous polymer-rich phase are negligible, due to the high viscosity ratio in our glassy dynamics model. Evidence for this assumption is provided in the Supporting Information. Of course, hydrodynamics can prove to be more significant in NIPS operating regimes where the continuous polymer-rich phase is not subject to early vitrification; such complexities, including the physical mechanisms behind the formation of macrovoids[25,26] and other membrane morphologies,[30,31] are left to future study.

After we submitted this manuscript for publication, we became aware of an article in press[32] that uses a similar NIPS model to our own, but targeted at a specific polymer-solvent-nonsolvent system.

Acknowledgement

We acknowledge financial support from Asahi Kasei Corporation, the Center for Materials for Water and Energy Systems (MWET), an Energy Frontier Research Center funded by the U.S. Department of Energy, Office of Science, Basic Energy Sciences under Award #DE-SC0019272, and from Brigham Young University. We acknowledge computational resources from the Center for Scientific Computing from the CNSI, MRL: an NSF MRSEC (DMR-1720256) and NSF CNS-1725797. JUG acknowledges financial support from the NSERC PGS-D scholarship program (Canada). We thank Prof. Hector D. Ceniceros (UC Santa Barbara) for helpful discussions regarding the numerical treatment of fluctuating simulations.

Supporting Information Available

Phase-field model and numerical methods; Derivation of the fluctutations scales; Simulation setup; Pore size analysis; Porosity analysis; Choosing the mobility contrast η_p/η_s; Formation of the finger-like structures in 2D; Propagation dynamics of the phase-separation and glass-transition fronts; Phase separation with hydrodynamics.

References

(1) Pendergast, M. M.; Hoek, E. M. A review of water treatment membrane nanotechnologies. *Energy and Environmental Science* **2011**, *4*, 1946–1971, DOI: 10.1039/c0ee00541j.

(2) Landsman, M. R. et al. Water Treatment: Are Membranes the Panacea? *Annual review of chemical and biomolecular engineering* **2020**, *11*, 559–585, DOI: 10.1146/annurev-chembioeng-111919-091940.

(3) Baker, R. W. *Membrane Technology and Applications*, 3rd ed.; John Wiley and Sons, Ltd: West Sussex, United Kingdom, 2012; pp 1–571.

(4) Guillen, G. R.; Pan, Y.; Li, M.; Hoek, E. M. V. Preparation and Characterization of Membranes Formed by Nonsolvent Induced Phase Separation: A Review. *Industrial and Engineering Chemistry Research* **2011**, *50*, 3798–3817.

(5) Wang, D.-M.; Lai, J.-Y. Recent advances in preparation and morphology control of polymeric membranes formed by nonsolvent induced phase separation. *Current Opinion in Chemical Engineering* **2013**, *2*, 229–237, DOI: 10.1016/j.coche.2013.04.003.

(6) Loeb, S.; Sourirajan, S. High flow porous membranes for separating water from saline solutions (US 3,133,132). 1964.

(7) Akthakul, A.; Scott, C. E.; Mayes, A. M.; Wagner, A. J. Lattice Boltzmann simulation of asymmetric membrane formation by immersion precipitation. *Journal of Membrane Science* **2005**, *249*, 213–226, DOI: 10.1016/j.memsci.2004.09.045.

(8) Hopp-Hirschler, M.; Nieken, U. Modeling of pore formation in phase inversion processes: Model and numerical results. *Journal of Membrane Science* **2018**, *564*, 820–831, DOI: 10.1016/j.memsci.2018.07.085.

(9) Zhou, B.; Powell, A. C. Phase field simulations of early stage structure formation during immersion precipitation of polymeric membranes in 2D and 3D. *J. Memb. Sci.* **2006**, *268*, 150–164, DOI: 10.1016/j.memsci.2005.05.030.

(10) Tree, D. R.; Delaney, K. T.; Ceniceros, H. D.; Iwama, T.; Fredrickson, G. H. A multi-fluid model for microstructure formation in polymer membranes. *Soft Matter* **2017**, *13*, 3013–3030, DOI: 10.1039/C6SM02839J.

(11) Tree, D. R.; Iwama, T.; Delaney, K. T.; Lee, J.; Fredrickson, G. H. Marangoni Flows during Nonsolvent Induced Phase Separation. *ACS Macro Letters* **2018**, *7*, 582–586, DOI: 10.1021/acsmacrolett.8b00012.

(12) Tree, D. R.; Dos Santos, L. F.; Wilson, C. B.; Scott, T. R.; Garcia, J. U.; Fredrickson, G. H. Mass-transfer driven spinodal decomposition in a ternary polymer solution. *Soft Matter* **2019**, *15*, 4614–4628, DOI: 10.1039/c9sm00355j.

(13) Cervellere, M. R.; Tang, Y.; Qian, X.; Ford, D. M.; Millett, P. C. Mesoscopic simulations of thermally-induced phase separation in PVDF/DPC solutions. *Journal of Membrane Science* **2019**, DOI: 10.1016/j.memsci.2019.02.014.

(14) van de Witte, P.; Dijkstra, P. J.; van den Berg, J. W. a.; Feijen, J. Phase separation processes in polymer solutions in relation to membrane formation. *Journal of Membrane Science* **1996**, *117*, 1–31, DOI: 10.1016/0376-7388(96)00088-9.

(15) Hohenberg, P. C.; Halperin, B. I. Theory of dynamic critical phenomena. *Reviews of Modern Physics* **1977**, *49*, 435–479, DOI: 10.1103/RevModPhys.49.435.

(16) Hiemenz, P. C.; Lodge, T. P. *Polymer Chemistry*, 2nd ed.; CRC Press: Boca Raton, 2007; pp 1–575.

(17) Li, S. G.; Van De Boomgaard, T.; Smolders, C. A.; Strathmann, H. Physical gelation of amorphous polymers in a mixture of solvent and nonsolvent. *Macromolecules* **1996**, *29*, 2053–2059, DOI: 10.1021/ma9508966.

(18) Kim, J. Y.; Kim, Y. D.; Kanamori, T.; Lee, H. K.; Baik, K.-j.; Kim, S. C. Vitrification Phenomena in Polysulfone / NMP / Water System. *Journal of Applied Polymer Science* **1998**, *71*, 431–438.

(19) Ball, R. C.; Essery, R. L. Spinodal decomposition and pattern formation near surfaces. *Journal of Physics: Condensed Matter* **1990**, *2*, 10303–10320, DOI: 10.1088/0953-8984/2/51/006.

(20) Lifshitz, I.; Slyozov, V. The kinetics of precipitation from supersaturated solid solutions. *Journal of Physics and Chemistry of Solids* **1961**, *19*, 35–50, DOI: 10.1016/0022-3697(61)90054-3.

(21) Wagner, C. Theorie der alterung von niederschlagen durch umlosen (Ostwald-reifung). *Zeitschrift fur elektrochemie* **1961**, 581–591.

(22) Koenhen, D. M.; Mulder, M. H. V.; Smolders, C. A. Phase separation phenomena during the formation of asymmetric membranes. *Journal of Applied Polymer Science* **1977**, *21*, 199–215, DOI: 10.1002/app.1977.070210118.

(23) Wijmans, J. G.; Baaij, J. P. B.; Smolders, C. A. The mechanism of formation of microporous or skinned membranes produced by immersion precipitation. *Journal of Membrane Science* **1983**, *14*, 263–274, DOI: 10.1016/0376-7388(83)80005-2.

(24) Wijmans, J. G.; Kant, J.; M, M. H. V.; Smolders, C. A. Phase separation phenomena in solutions of polysulfone in mixtures of a solvent and a nonsolvent : relationship with membrane formation. *Polymer* **1985**, *26*, 1539–1545.

(25) Smolders, C. A.; Reuvers, A. J.; Boom, R. M.; Wienk, I. M. Microstructures in phase-inversion membranes. Part 1. Formation of macrovoids. *Journal of Membrane Science* **1992**, *73*, 259–275, DOI: 10.1016/0376-7388(92)80134-6.

(26) Wang, H. H.; Jung, J. T.; Kim, J. F.; Kim, S.; Drioli, E.; Lee, Y. M. A novel green solvent alternative for polymeric membrane preparation via nonsolvent-induced phase separation (NIPS). *Journal of Membrane Science* **2019**, *574*, 44–54, DOI: 10.1016/j.memsci.2018.12.051.

(27) McHugh, A. J.; Tsay, C. S. Dynamics of the Phase Inversion Process. *J. Appl. Polym. Sci.* **1992**, *46*, 2011–2021.

(28) Strathmann, H.; Kock, K.; Amar, P.; Baker, R. W. The formation mechanism of asymmetric membranes. *Desalination* **1975**, *16*, 179–203, DOI: 10.1016/S0011-9164(00)82092-5.

(29) Radovanovic, P.; Thiel, S. W.; Hwang, S. T. Formation of asymmetric polysulfone membranes by immersion precipitation. Part II. The effects of casting solution and gelation bath compositions on membrane structure and skin formation. *J. Memb. Sci.* **1992**, *65*, 231–246, DOI: 10.1016/0376-7388(92)87025-S.

(30) Cardoso, V. F.; Botelho, G.; Lanceros-Méndez, S. Nonsolvent induced phase separation preparation of poly(vinylidene fluoride-co-chlorotrifluoroethylene) membranes with tailored morphology, piezoelectric phase content and mechanical properties. *Materials and Design* **2015**, *88*, 390–397, DOI: 10.1016/j.matdes.2015.09.018.

(31) Jung, J. T.; Kim, J. F.; Wang, H. H.; di Nicolo, E.; Drioli, E.; Lee, Y. M. Understanding the non-solvent induced phase separation (NIPS) effect during the fabrication of mi-

croporous PVDF membranes via thermally induced phase separation (TIPS). *Journal of Membrane Science* **2016**, *514*, 250–263, DOI: 10.1016/j.memsci.2016.04.069.

(32) Cervellere, M. R.; Qian, X.; Ford, D. M.; Carbrello, C.; Giglia, S.; Millett, P. C. Phase-field modeling of non-solvent induced phase separation (NIPS) for PES/NMP/Water with comparison to experiments. *Journal of Membrane Science* **2020**, DOI: https://doi.org/10.1016/j.memsci.2020.118779.

Graphical TOC Entry

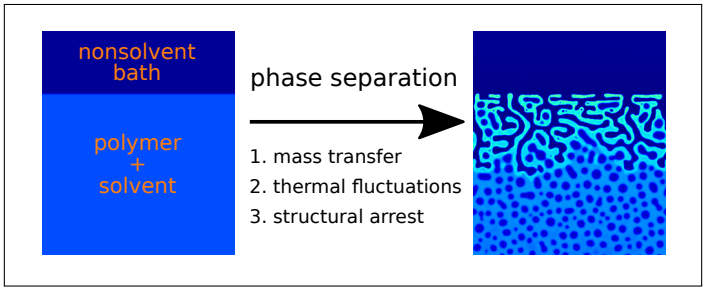

Supporting Information: Mechanisms of Asymmetric Membrane Formation in Nonsolvent-Induced Phase Separation

Jan Ulric Garcia,[†,‡] Tatsuhiro Iwama,[¶] Eva Y. Chan,[†] Douglas R. Tree,[§] Kris T. Delaney,[‡] and Glenn H. Fredrickson[*,†,‡,‖]

†*Dept. of Chemical Engineering, University of California, Santa Barbara, CA 93106, USA*

‡*Materials Research Laboratory, University of California, Santa Barbara, CA 93106, USA*

¶*Asahi Kasei Corporation, 2-1 Samejima, Fuji, Shizuoka 416-8501, Japan*

§*Dept. of Chemical Engineering, Brigham Young University, Provo, UT 84602, USA*

‖*Dept. of Materials, University of California, Santa Barbara, CA 93106, USA*

E-mail: ghf@ucsb.edu

Phase-field model and numerical methods

In our previous work,[S1] we presented the derivation of the following dimensional multi-component phase-field model using the Doi-Onuki formalism:[S2]

$$\frac{\partial \phi_i}{\partial t} + \boldsymbol{v} \cdot \boldsymbol{\nabla} \phi_i = \boldsymbol{\nabla} \cdot \left[\sum_j^{p,n} M_{ij} \boldsymbol{\nabla} \mu_j \right] \tag{1}$$

$$-\boldsymbol{\nabla} p + \boldsymbol{\nabla} \cdot \left[\eta (\boldsymbol{\nabla} \boldsymbol{v} + \boldsymbol{\nabla} \boldsymbol{v}^T) \right] = \boldsymbol{\nabla} \cdot \boldsymbol{\Pi} \tag{2}$$

$$\boldsymbol{\nabla} \cdot \boldsymbol{v} = 0 \tag{3}$$

where ϕ_p and ϕ_n are the polymer and nonsolvent volume fractions, respectively, the solvent volume fraction is implicitly determined from the incompressibility assumption, $\phi_s = 1 - \phi_p - \phi_n$, t is time, p is pressure, η is the viscosity, $\mathbf{\Pi}$ is the osmotic stress tensor, and M_{ij} is the matrix of mobility coefficients:

$$M_{pp} = \frac{b^2}{\eta_s}\phi_p(1-\phi_p) \tag{4a}$$

$$M_{pn} = M_{np} = -\frac{b^2}{\eta_s}\phi_p\phi_n \tag{4b}$$

$$M_{nn} = \frac{b^2}{\eta_s}\phi_n(1-\phi_n), \tag{4c}$$

whose definition follows from the assumption of local Rouse-like friction coefficients,

$$\zeta_i = b^{-3}\zeta_0\phi_i \tag{5}$$

where b is the length of a monomer and ζ_0 is the Stokes friction coefficient in a dilute solution of viscosity, η_s:

$$\zeta_0 = \eta_s b. \tag{6}$$

In this study, in lieu of the constant solvent viscosity in Eq 6, we use the concentration-dependent mixture viscosity for the Stokes friction:

$$\zeta_0 = \eta(\phi_p)b, \tag{7}$$

which then leads to the concentration-dependent-viscosity-scaled mobility model:

$$M_{pp} = \frac{b^2}{\eta(\phi_p)}\phi_p(1-\phi_p) \tag{8a}$$

$$M_{pn} = M_{np} = -\frac{b^2}{\eta(\phi_p)}\phi_p\phi_n \tag{8b}$$

$$M_{nn} = \frac{b^2}{\eta(\phi_p)}\phi_n(1-\phi_n). \tag{8c}$$

We also add mass and momentum fluctuations[S3,S4] to the dimensional model:

$$\frac{\partial \phi_i}{\partial t} + \boldsymbol{v} \cdot \boldsymbol{\nabla} \phi_i = \boldsymbol{\nabla} \cdot \left[\sum_j^{p,n} M_{ij} \boldsymbol{\nabla} \mu_j \right] + \alpha_\theta \theta_i(\boldsymbol{r}, t) \tag{9}$$

$$-\boldsymbol{\nabla} p + \boldsymbol{\nabla} \cdot \left[\eta (\boldsymbol{\nabla} \boldsymbol{v} + \boldsymbol{\nabla} \boldsymbol{v}^T) \right] = \boldsymbol{\nabla} \cdot \boldsymbol{\Pi} + \alpha_\xi \boldsymbol{\xi}(\boldsymbol{r}, t), \tag{10}$$

where α_θ and α_ξ are noise-scaling factors for the mass and momentum fluctuations, θ_i and $\boldsymbol{\xi}$, respectively, that follow fluctuation-dissipation theorem statistics,

$$\langle \theta_i(\boldsymbol{r}, t) \rangle = 0 \tag{11a}$$

$$\langle \xi_k(\boldsymbol{r}, t) \rangle = 0 \tag{11b}$$

$$\langle \theta_i(\boldsymbol{r}, t) \theta_j(\boldsymbol{r'}, t') \rangle = -2 k_B T \boldsymbol{\nabla} \cdot [M_{ij}(\boldsymbol{r}) \boldsymbol{\nabla} \delta(\boldsymbol{r} - \boldsymbol{r'})] \delta(t - t') \tag{11c}$$

$$\langle \xi_k(\boldsymbol{r}, t) \xi_l(\boldsymbol{r'}, t') \rangle = -2 k_B T \delta_{kl} \boldsymbol{\nabla} \cdot [\eta(\boldsymbol{r}) \boldsymbol{\nabla} \delta(\boldsymbol{r} - \boldsymbol{r'})] \delta(t - t'), \tag{11d}$$

where the indices i and j refer to species components while k and l refer to dimensional components. To nondimensionalize our model, we use R_0, the root-mean-square (RMS) end-to-end distance of a reference polymer with degree of polymerization N_r as the characteristic length scale ($R_0 = b N_r^{1/2}$), τ, the Rouse time of the reference polymer in a solvent of viscosity, η_s, as the characteristic time scale ($\tau = N_r^2 \eta_s b^3 / k_B T$), b^2/η_s as the characteristic mobility scale, $N_r k_B T / b^3$ as the characteristic chemical potential scale, and η_s / τ as the characteristic pressure scale; we determined the characteristic scales for the mass and momentum fluctuations as $\theta_c = N_r^{-1/4}/\tau$ and $\xi_c = k_B T / R^{5/2} N_r b^{3/2}$, respectively, as shown in the next section. Following nondimensionalization, we end up with the following model where tildes mark scaled quantities:

$$\frac{\partial \phi_i}{\partial \widetilde{t}} + \widetilde{\boldsymbol{v}} \cdot \widetilde{\boldsymbol{\nabla}} \phi_i = \widetilde{\boldsymbol{\nabla}} \cdot \left[\sum_j^{p,n} \widetilde{M_{ij}} \widetilde{\boldsymbol{\nabla}} \widetilde{\mu_j} \right] + \alpha_\theta N_r^{-1/4} \widetilde{\theta_i}\left(\widetilde{\boldsymbol{r}}, \widetilde{t}\right) \tag{12}$$

$$-\widetilde{\boldsymbol{\nabla}} \widetilde{p} + \widetilde{\boldsymbol{\nabla}} \cdot \left[\widetilde{\eta} (\widetilde{\boldsymbol{\nabla}} \widetilde{\boldsymbol{v}} + \widetilde{\boldsymbol{\nabla}} \widetilde{\boldsymbol{v}}^T) \right] = N_r \widetilde{\boldsymbol{\nabla}} \cdot \widetilde{\boldsymbol{\Pi}} + \alpha_\xi N_r^{1/4} \widetilde{\boldsymbol{\xi}}\left(\widetilde{\boldsymbol{r}}, \widetilde{t}\right) \tag{13}$$

where $\widetilde{\theta}_i$ and $\widetilde{\boldsymbol{\xi}}$ are Gaussian-distributed noise that follow nondimensional fluctuation-dissipation theorem statistics,

$$\langle\widetilde{\theta}_i\big(\widetilde{\boldsymbol{r}},\widetilde{t}\big)\rangle = 0 \tag{14a}$$

$$\langle\widetilde{\xi}_k\big(\widetilde{\boldsymbol{r}},\widetilde{t}\big)\rangle = 0 \tag{14b}$$

$$\langle\widetilde{\theta}_i\big(\widetilde{\boldsymbol{r}},\widetilde{t}\big)\widetilde{\theta}_j\big(\widetilde{\boldsymbol{r}}',\widetilde{t}'\big)\rangle = -2\widetilde{\boldsymbol{\nabla}}\cdot\Big[\widetilde{M_{ij}}(\widetilde{\boldsymbol{r}})\widetilde{\boldsymbol{\nabla}}\delta(\widetilde{\boldsymbol{r}}-\widetilde{\boldsymbol{r}}')\Big]\delta\big(\widetilde{t}-\widetilde{t}'\big) \tag{14c}$$

$$\langle\widetilde{\xi}_k\big(\widetilde{\boldsymbol{r}},\widetilde{t}\big)\widetilde{\xi}_l\big(\widetilde{\boldsymbol{r}}',\widetilde{t}'\big)\rangle = -2\delta_{kl}\widetilde{\boldsymbol{\nabla}}\cdot\Big[\widetilde{\eta}(\widetilde{\boldsymbol{r}})\widetilde{\boldsymbol{\nabla}}\delta(\widetilde{\boldsymbol{r}}-\widetilde{\boldsymbol{r}}')\Big]\delta\big(\widetilde{t}-\widetilde{t}'\big), \tag{14d}$$

where the indices i and j refer to species components while k and l refer to dimensional components. For computational efficiency in calculating thermal fluctuations, we allow for local dependence of $\widetilde{M_{ij}}$ and $\widetilde{\eta}$ but assume zero gradient:

$$\langle\widetilde{\theta}_i\big(\widetilde{\boldsymbol{r}},\widetilde{t}\big)\widetilde{\theta}_j\big(\widetilde{\boldsymbol{r}}',\widetilde{t}'\big)\rangle \approx -2\widetilde{M_{ij}}(\widetilde{\boldsymbol{r}})\widetilde{\nabla^2}\delta(\widetilde{\boldsymbol{r}}-\widetilde{\boldsymbol{r}}')\delta\big(\widetilde{t}-\widetilde{t}'\big) \tag{15a}$$

$$\langle\widetilde{\xi}_k\big(\widetilde{\boldsymbol{r}},\widetilde{t}\big)\widetilde{\xi}_l\big(\widetilde{\boldsymbol{r}}',\widetilde{t}'\big)\rangle \approx -2\delta_{kl}\widetilde{\eta}(\widetilde{\boldsymbol{r}})\widetilde{\nabla^2}\delta(\widetilde{\boldsymbol{r}}-\widetilde{\boldsymbol{r}}')\delta\big(\widetilde{t}-\widetilde{t}'\big). \tag{15b}$$

For this paper, we limit our scope to diffusion-only dynamics by setting all velocities to zero, simplifying our nondimensional model to

$$\frac{\partial\phi_i}{\partial\widetilde{t}} = \widetilde{\boldsymbol{\nabla}}\cdot\left[\sum_j^{p,n}\widetilde{M_{ij}}\widetilde{\boldsymbol{\nabla}}\widetilde{\mu}_j\right] + \alpha N_r^{-1/4}\widetilde{\theta}_i\big(\widetilde{\boldsymbol{r}},\widetilde{t}\big), \tag{16}$$

where the nondimensional mobility matrix is defined as

$$\widetilde{M_{pp}} = \phi_p(1-\phi_p)/\widetilde{\eta}(\phi_p) \tag{17a}$$

$$\widetilde{M_{pn}} = \widetilde{M_{np}} = -\phi_p\phi_n/\widetilde{\eta}(\phi_p) \tag{17b}$$

$$\widetilde{M_{nn}} = \phi_n(1-\phi_n)/\widetilde{\eta}(\phi_p), \tag{17c}$$

where $\widetilde{\eta}(\phi_p) = \eta(\phi_p)/\eta_s$. The noise-scaling factor is simplified to $\alpha = \alpha_\theta$ due to the absence of momentum fluctuations in Eq 16. While the Stokes equation (Eq 10) is not needed in this

limit, the local viscosity, $\widetilde{\eta}$, remains as a factor scaling the mobilities in Eq 17. In the main manuscript, we report all equations in their nondimensional form, allowing us to drop the tildes for convenience.

We used a pseudo-spectral method with semi-implicit time-stepping to solve Eq 16. Spatial discretization is set uniformly in each dimension as one discretization point per unit length, R_0, *e.g.,* $L_x/N_x = R_0$, $L_y/N_y = R_0$ for 2D simulations. We used constant time-stepping with $\Delta t = 0.001$ and $\alpha = 0.04$. Simulations were carried out using our custom phase-field software. Our methods paper[S1] includes more details of the requisite numerical techniques.

Derivation of the fluctuations scales

We determined the characteristic scale for mass fluctuations, θ_c, by nondimensionalizing Eq 11c using the same characteristic quantities in the preceding section.

$$\langle \theta_i(\boldsymbol{r},t)\theta_j(\boldsymbol{r'},t')\rangle = -2k_BT\boldsymbol{\nabla}\cdot[M_{ij}(\boldsymbol{r})\boldsymbol{\nabla}\delta(\boldsymbol{r}-\boldsymbol{r'})]\delta(t-t') \tag{18}$$

$$= k_BT\frac{b^2}{\eta_s R_0^5\tau}\Big(-2\widetilde{\boldsymbol{\nabla}}\cdot\Big[\widetilde{M_{ij}}(\widetilde{\boldsymbol{r}})\widetilde{\boldsymbol{\nabla}}\delta(\widetilde{\boldsymbol{r}}-\widetilde{\boldsymbol{r'}})\Big]\delta\big(\widetilde{t}-\widetilde{t'}\big)\Big) \tag{19}$$

$$= \frac{k_BT}{N_r^2\eta_s b^3}\frac{N_r^{-1/2}}{\tau}\Big(-2\widetilde{\boldsymbol{\nabla}}\cdot\Big[\widetilde{M_{ij}}(\widetilde{\boldsymbol{r}})\widetilde{\boldsymbol{\nabla}}\delta(\widetilde{\boldsymbol{r}}-\widetilde{\boldsymbol{r'}})\Big]\delta\big(\widetilde{t}-\widetilde{t'}\big)\Big) \tag{20}$$

$$= \frac{N_r^{-1/2}}{\tau^2}\Big(-2\widetilde{\boldsymbol{\nabla}}\cdot\Big[\widetilde{M_{ij}}(\widetilde{\boldsymbol{r}})\widetilde{\boldsymbol{\nabla}}\delta(\widetilde{\boldsymbol{r}}-\widetilde{\boldsymbol{r'}})\Big]\delta\big(\widetilde{t}-\widetilde{t'}\big)\Big) \tag{21}$$

$$= \theta_c^2\langle\widetilde{\theta}_i\big(\widetilde{\boldsymbol{r}},\widetilde{t}\big)\widetilde{\theta}_j\big(\widetilde{\boldsymbol{r'}},\widetilde{t'}\big)\rangle. \tag{22}$$

Thus, we have shown that,

$$\theta_c = \frac{N_r^{-1/4}}{\tau} \tag{23}$$

Similarly, we determined the characteristic scale for momentum fluctuations, ξ_c, by nondimensionalizing Eq 11d using the same characteristic quantities in the preceding section.

$$\langle \xi_k(\boldsymbol{r},t)\xi_l(\boldsymbol{r'},t')\rangle = -2k_BT\delta_{kl}\boldsymbol{\nabla}\cdot[\eta(\boldsymbol{r})\boldsymbol{\nabla}\delta(\boldsymbol{r}-\boldsymbol{r'})]\delta(t-t') \tag{24}$$

$$= \frac{k_BT\eta_s}{R_0^5\tau}\Big(-2\delta_{kl}\widetilde{\boldsymbol{\nabla}}\cdot\Big[\widetilde{\eta}(\widetilde{\boldsymbol{r}})\widetilde{\boldsymbol{\nabla}}\delta(\widetilde{\boldsymbol{r}}-\widetilde{\boldsymbol{r}'})\Big]\delta\big(\widetilde{t}-\widetilde{t'}\big)\Big) \tag{25}$$

$$= \frac{(k_BT)^2}{R_0^5N_r^2b^3}\Big(-2\delta_{kl}\widetilde{\boldsymbol{\nabla}}\cdot\Big[\widetilde{\eta}(\widetilde{\boldsymbol{r}})\widetilde{\boldsymbol{\nabla}}\delta(\widetilde{\boldsymbol{r}}-\widetilde{\boldsymbol{r}'})\Big]\delta\big(\widetilde{t}-\widetilde{t'}\big)\Big) \tag{26}$$

$$= \xi_c^2\langle\widetilde{\xi_k}\big(\widetilde{\boldsymbol{r}},\widetilde{t}\big)\widetilde{\xi_l}\big(\widetilde{\boldsymbol{r}'},\widetilde{t'}\big)\rangle. \tag{27}$$

Thus, we have shown that,

$$\xi_c = \frac{k_BT}{R_0^{5/2}N_rb^{3/2}}. \tag{28}$$

Simulation setup

In 2D, we set a simulation box of size, $512R_0 \times 2048R_0$ as shown in Figure S1. As we use Fourier transforms to calculate the spatial derivatives, we set periodic boundary conditions on all sides of the simulation box. To establish no-flux boundary conditions at the bottom of the film and at the top of the bath, we initialize the concentrations to be symmetric across the midpoint, $y = 1024$. For each vertical half of the simulation box, we set the inner half as the initial film and the outer half as the nonsolvent bath. In the main manuscript, we showed only the domains corresponding to the film at the top-half of the simulation box. Pore-size profiling was also limited to the shown domain. Though we set the initial film composition to be symmetric along the y-axis, we did not symmetrize the thermal fluctuations, resulting in the microstructures for the two halves to not be identical, and in fact, they constitute independent statistical realizations of the film and bath dynamics. Nevertheless, the no-flux boundary conditions at the bottom of the film and at the top of the bath are satisfied, as shown in Figure S1. We use the same setup in 3D with a total simulation box size of $64R_0 \times 512R_0 \times 64R_0$.

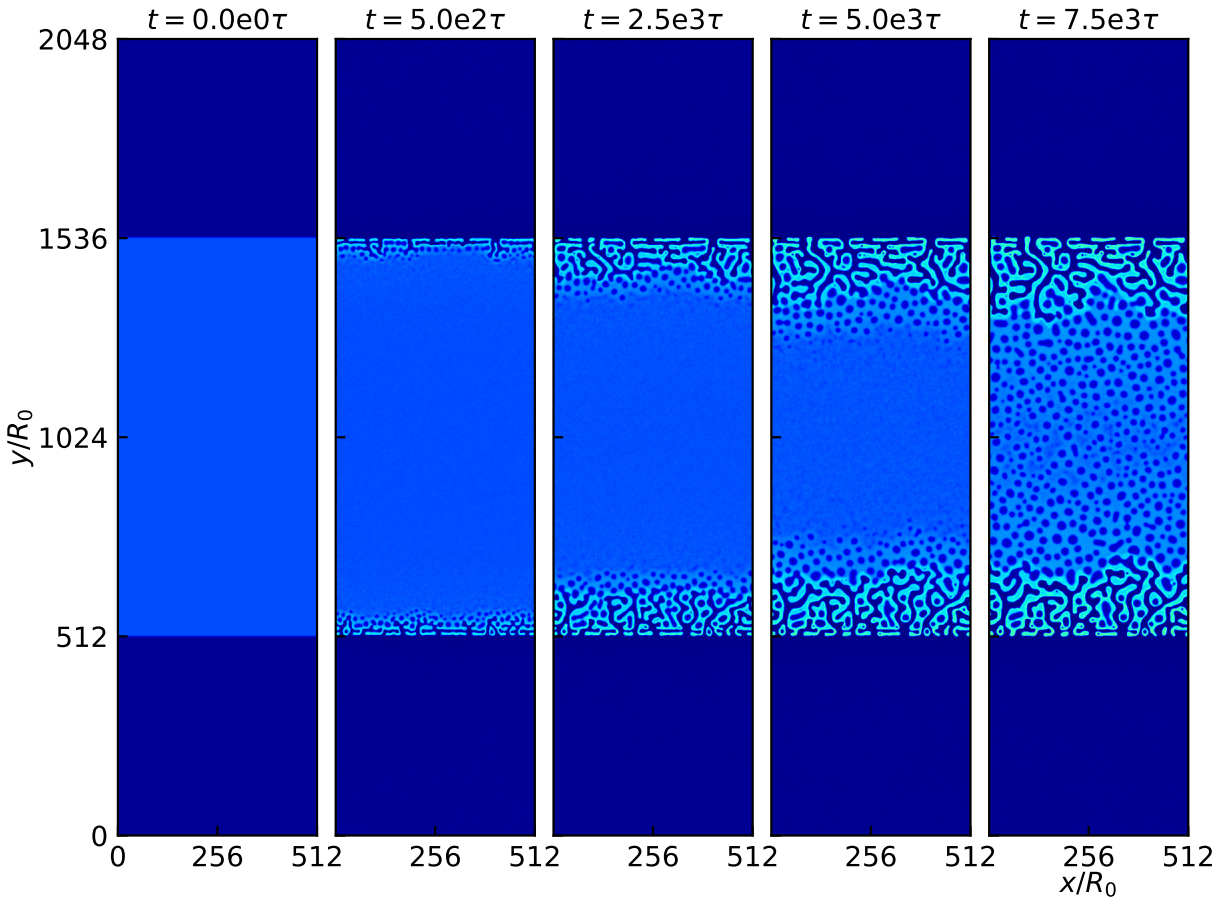

Figure S1: NIPS simulations in 2D, showing the entire simulation box, with glass transition effects ($\eta_p/\eta_s = 10^4$) for the initial film composition of ($\phi_p = 0.20, \phi_n = 0.45$), corresponding to the green triangle in Figure 1. Polymer-rich regions are light green and polymer-poor regions are dark blue, ϕ_p color bar included in Figure 2.

Pore size analysis

We calculate the polymer structure factor for each lateral slice of the film: for 2D simulations, these are structure factors of 1D slices along the y-axis; for 3D simulations, the computed structure factors are 2D slices along the y-axis,

$$S_p(\boldsymbol{q}, y) = \frac{1}{V} \sum_{\boldsymbol{r}} \sum_{\boldsymbol{r'}} e^{-i\boldsymbol{q}\cdot\boldsymbol{r}} \left[\phi_p(\boldsymbol{r}+\boldsymbol{r'}, y)\phi_p(\boldsymbol{r'}, y) - \langle\phi_p\rangle^2\right] \tag{29}$$

where V is the number of lattice points for that specific y-slice, and $\boldsymbol{r}$, $\boldsymbol{r'}$, and $\boldsymbol{q}$ are vectors in the $x-z$ plane. The second moment of $S_p(\boldsymbol{q}, y)$ for each y-slice,

$$\left\langle q^2(y)\right\rangle = \frac{\sum\limits_{\boldsymbol{q}} (\boldsymbol{q}\cdot\boldsymbol{q}) S_p(\boldsymbol{q}, y)}{\sum\limits_{\boldsymbol{q}} S_p(\boldsymbol{q}, y)}, \tag{30}$$

is used to estimate the characteristic domain size, L, by means of

$$L(y) = \frac{2\pi}{\left\langle q^2(y)\right\rangle^{1/2}}. \tag{31}$$

The approach described above is more robust than the traditional method of calculating $\langle q\rangle$ from the 1D histogram of the n-dimensional structure factor $S_p(\boldsymbol{q})$. The calculated value of L using the traditional method is highly sensitive to the number of bins used for the histogram, especially in simulations where the number of lattice points per slice is limited.

Porosity analysis

Figure S2 shows the porosity profiles of the 3D membranes shown in Figures 5 and 6. To calculate porosity, a threshold was applied to the density fields to make them binary. We set the threshold arbitrarily to $\phi_p^{thresh} = 0.90\phi_p^*$, *i.e.,* any domain where $\phi_p < \phi_p^{thresh}$ was considered "porous." Porosity was then calculated as the fraction of porous domains. Using this metric, the entire film starts as completely porous as nothing hinders the entry of nonsol-

vent. As NIPS proceeds, the polymer-rich membrane matrix forms, reducing film porosity. Porosity itself is distinct from pore size; two cross-sections can have the same porosity but exhibit different characteristic pore sizes. Note that we hold more confidence in our pore size analysis than our porosity calculations; we found that porosity is relatively sensitive to the value of ϕ_p^{thresh}, especially for the limited lateral dimensions of our simulations.

Choosing the mobility contrast η_p/η_s

As discussed in the main manuscript, we model the viscosity as a sigmoidal function of the local polymer volume fraction, $\phi_p(\boldsymbol{r})$:

$$\eta = 1 + \frac{\eta_p/\eta_s - 1}{1 + \exp\left(-\frac{1}{w}\left(\phi_p(\boldsymbol{r}) - \phi_p^*\right)\right)} \tag{32}$$

where w is the width of the sigmoid, ϕ_p^* is the glass-transition concentration, and η_p/η_s is the effective contrast in local mobilities between the glassy and non-glassy regions. The sigmoidal model mimics the exponential growth in the viscosity of polymer solutions as predicted by the well-known Vogel-Fulcher-Tamman-Hesse (VFTH) and Williams-Landel-Ferry (WLF) equations[S5] while bounding the maximum η for computational stability. We need to set η_p/η_s high enough that the sigmoidal model faithfully represents a physical glass transition. On the other hand, we cannot choose an exceedingly high value for η_p/η_s as it will slow down microstructure evolution excessively such that we cannot observe physically meaningful dynamics in accessible simulation times.

Figure S3 shows a bulk spinodal quench in 1D for different values of η_p/η_s. At $t = 15.8$, the concentrations are practically identical. However, by $t = 10^2$, the polymer-rich phase concentration for $\eta_p/\eta_s = 1$ has reached equilibrium, crossing the glass transition, ϕ_p^* on the way. We expect this behavior since setting $\eta_p/\eta_s = 1$ disables the glass transition. Meanwhile, the polymer-rich phase concentrations for $\eta_p/\eta_s = 10^4$ and $\eta_p/\eta_s = 10^6$ are approaching ϕ_p^* but have not crossed its value, as expected of a physical glass transition.

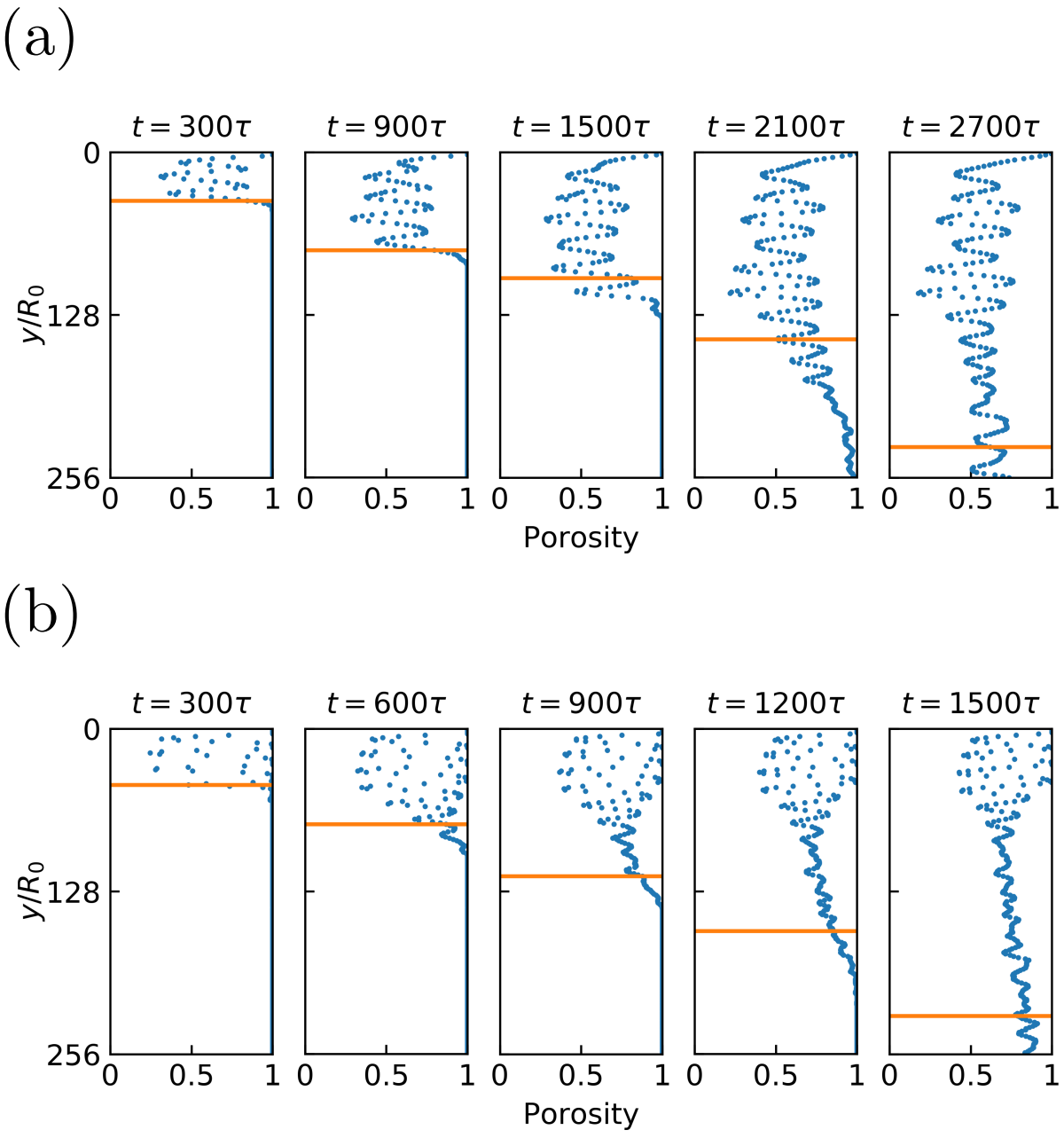

Figure S2: Porosity profiles for the 3D NIPS simulations shown in (a) Figure 5 and (b) Figure 6. The orange line reprsents the glass-transition front.

However, by $t = 10^3$, the polymer-rich phase concentration for $\eta_p/\eta_s = 10^4$ has crossed ϕ_p^*, and the polymer-rich phase becomes even more enriched by $t = 10^4$, although it has still not reached the equilibrium value. On the other hand, the polymer-rich phase concentration for $\eta_p/\eta_s = 10^6$ barely crossed ϕ_p^* even by $t = 10^4$.

Based on Figure S3, setting $\eta_p/\eta_s = 10^6$ would be preferred. In fact, some experimental studies of membrane formation characterize a gel as a fluid with viscosity, 10^6 centipoise.[S6,S7] However, we see that the polymer-rich phase concentration crossing ϕ_p^* does not qualitatively change the coarse features of the NIPS microstructures shown in Figures S4 and S5. Choosing $\eta_p/\eta_s = 10^6$ leads to sharper interfaces for the finger-like structures shown in Figure S4 but doing so significantly slows down microstructure evolution. Meanwhile, we observe no large-scale morphological differences between the two levels of viscosity contrast in Figure S5. Thus, we choose to set $\eta_p/\eta_s = 10^4$, trading fine microstructural features for faster microstructure evolution for at least one film composition in 2D.

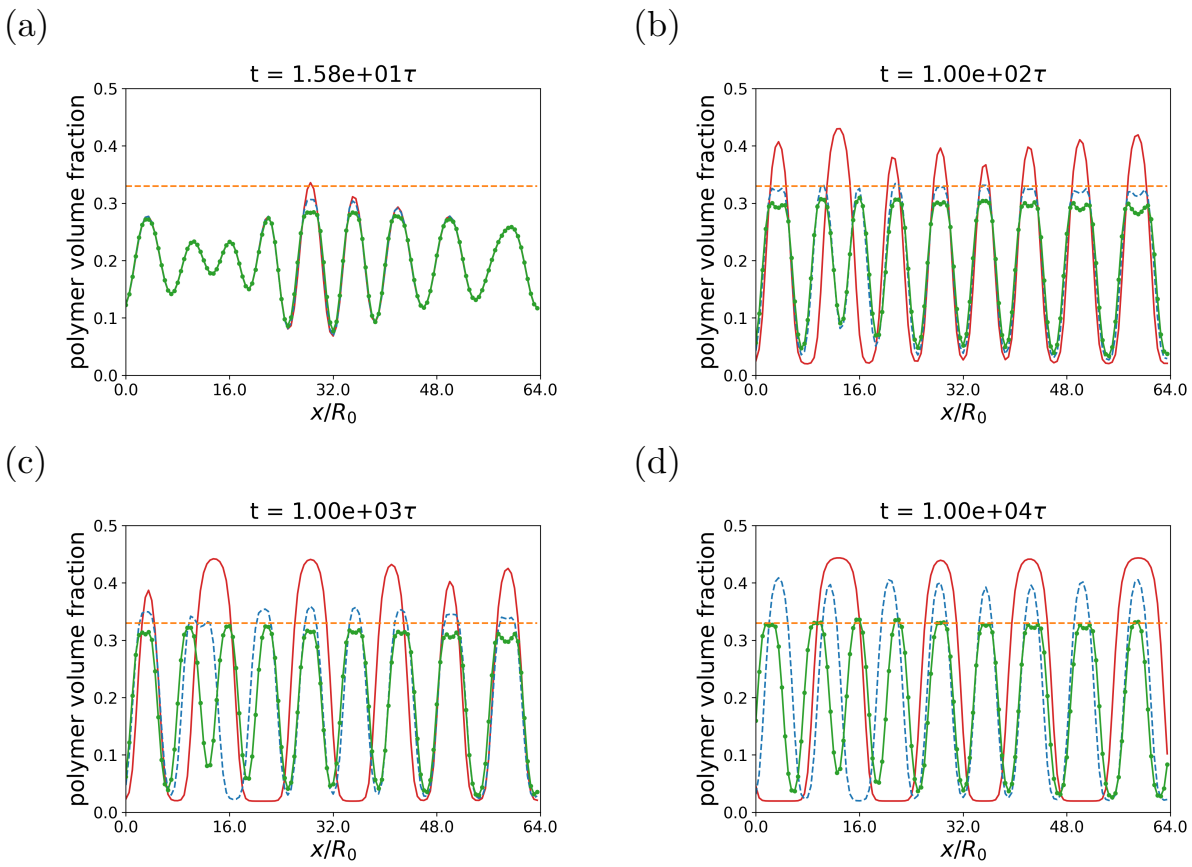

Figure S3: Spinodal quench ($\phi_p = 0.20, \phi_n = 0.45$) in 1D using the same thermodynamic parameters in this study for simulations of different mobility contrasts: $\eta_p/\eta_s = 10^0$ (solid red line), $\eta_p/\eta_s = 10^4$ (dashed blue line), $\eta_p/\eta_s = 10^6$ (dotted green line). The dashed orange line marks the glass transition concentration, ϕ_p^*. Different panels correspond to different simulation times, (a) $t = 15.8$, (b) $t = 10^2$, (c) $t = 10^3$, (d) $t = 10^4$.

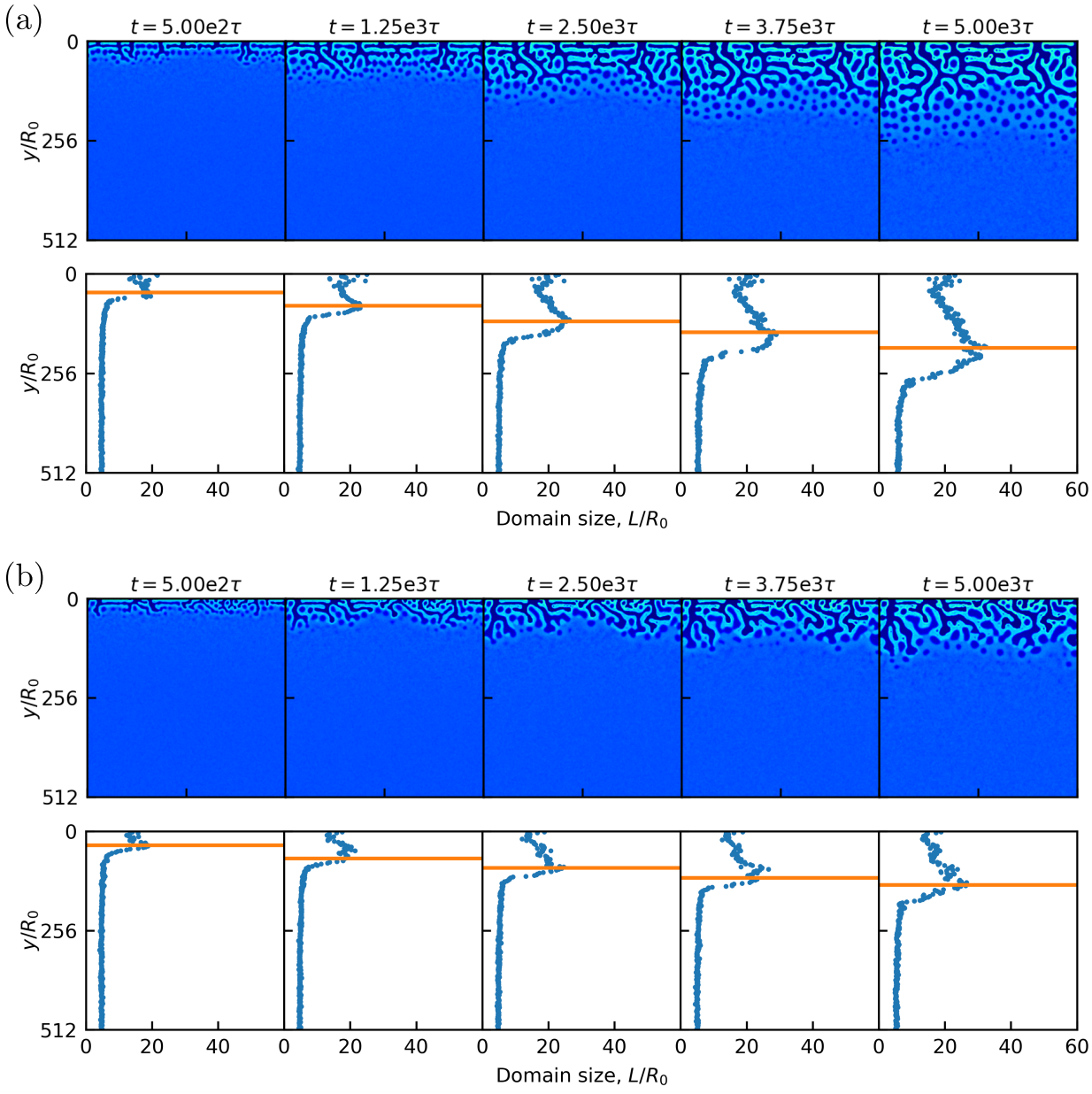

Figure S4: NIPS simulations in 2D and their domain size profiles for the initial film composition of $(\phi_p = 0.20, \phi_n = 0.45)$, corresponding to the green triangle in Figure 1. Mobility contrasts set at (a) $\eta_p/\eta_s = 10^4$, (b) $\eta_p/\eta_s = 10^6$. Each density plot shown is $512R_0 \times 512R_0$. The y-coordinate corresponds to film depth, where $y = 0$ is the film-bath interface and $y = 512$ is the bottom of the film. Polymer-rich regions are light green and polymer-poor regions are dark blue, ϕ_p color bar included in Figure 2. The orange line (glass-transition front) in the domain size profile corresponds to the deepest point in the film where at least one grid point has crossed the glass transition concentration, ϕ_p^*.

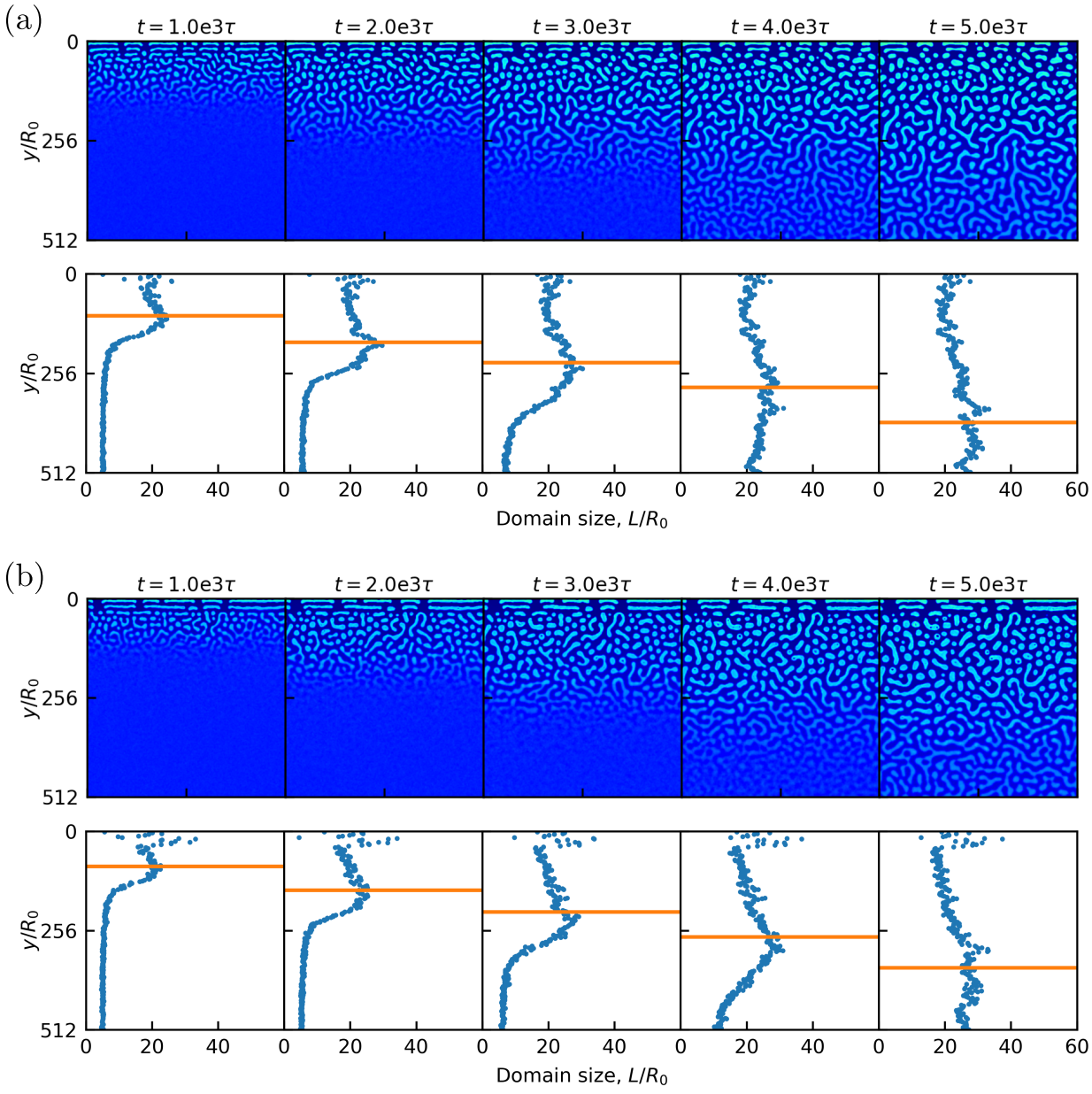

Figure S5: NIPS simulations in 2D and their domain size profiles for the initial film composition of ($\phi_p = 0.15, \phi_n = 0.50$), corresponding to the green square in Figure 1. Mobility contrasts set at (a) $\eta_p/\eta_s = 10^4$, (b) $\eta_p/\eta_s = 10^6$. Each density plot shown is $512R_0 \times 512R_0$. The y-coordinate corresponds to film depth, where $y = 0$ is the film-bath interface and $y = 512$ is the bottom of the film. Polymer-rich regions are light green and polymer-poor regions are dark blue, ϕ_p color bar included in Figure 2. The orange line (glass-transition front) in the domain size profile corresponds to the deepest point in the film where at least one grid point has crossed the glass transition concentration, ϕ_p^*.

Formation of the finger-like structures in 2D

We include a close-up view of the formation of the finger-like structures at early times in Figure S6. These images come from the same simulation as Figure 3b.

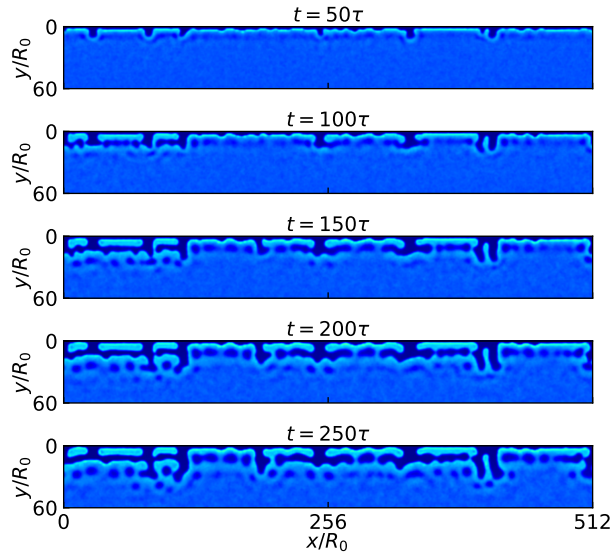

Figure S6: Formation of finger-like structures at early times in 2D corresponding to the simulation in Figure 3b. Polymer-rich regions are light green and polymer-poor regions are dark blue, ϕ_p color bar included in Figure 2.

Propagation dynamics of the phase-separation and glass-transition fronts

We plot the advance of the phase-separation and glass-transition fronts for all the NIPS simulations with a glass transition included in the main manuscript. We determined the location of the phase-separation front as the deepest point in the film where the difference between the maximum and minimum polymer concentrations crosses a heuristic threshold. In this analysis, we set this threshold at $\phi_p^{max} - \phi_p^{min} = 0.1$. We recorded the glass-transition front as the deepest point in the film where at least one pixel (or voxel) has crossed the glass transition concentration, ϕ_p^*. In all figures included, the lead of the phase-separation

front on the glass-transition front increases with time, allowing for the formation of the graded asymmetric pore size distributions. In 2D, the phase-separation and glass-transition fronts travel slower for the dope composition that leads to a polymer-rich matrix, evident in comparing Figure S7a and Figure S7b. Due to the greater tendency of forming bicontinuous structures, the composition dependence of the speed of the fronts is reduced in 3D as shown by comparing Figure S8a and Figure S8b. Overall, both fronts travel faster in 3D than in 2D.

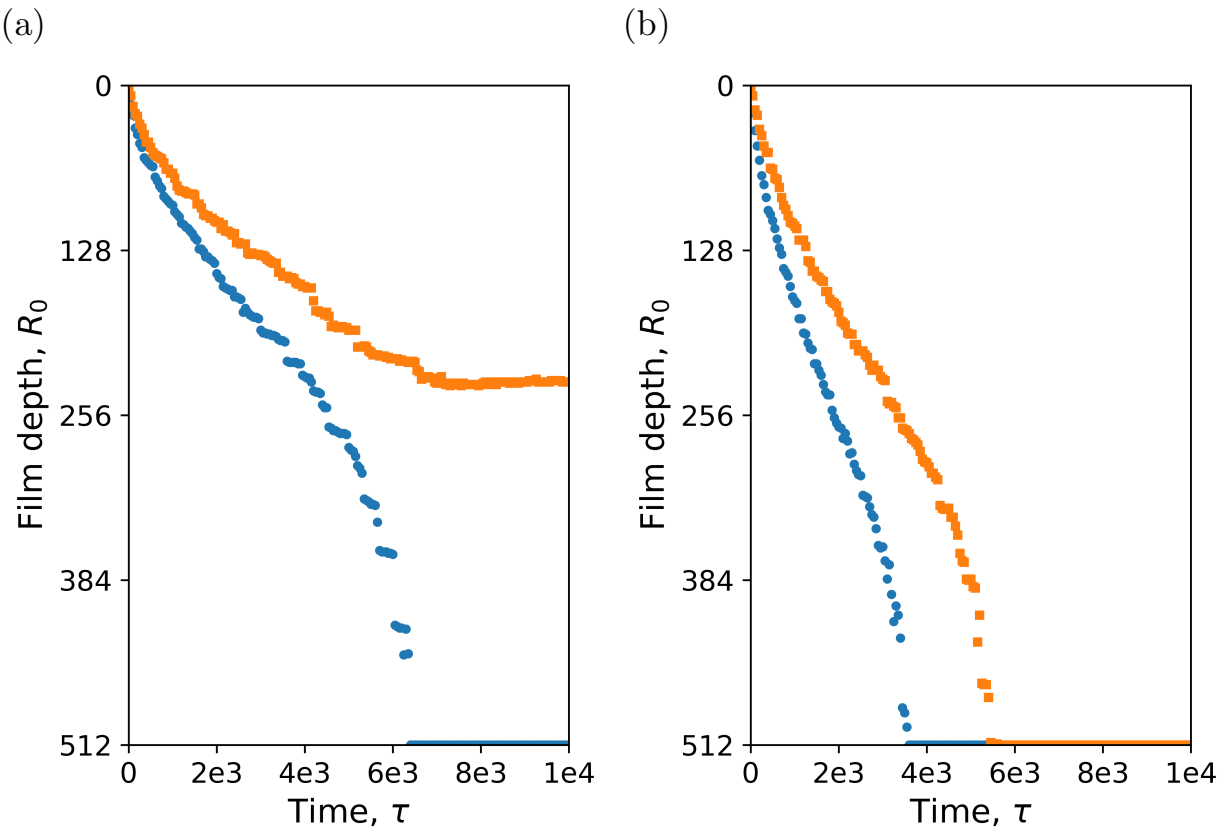

Figure S7: Propagation dynamics of the phase-separation (blue circles) and glass-transition (orange squares) fronts into the film for the 2D NIPS simulations shown in (a) Figure 3b and (b) Figure 4b.

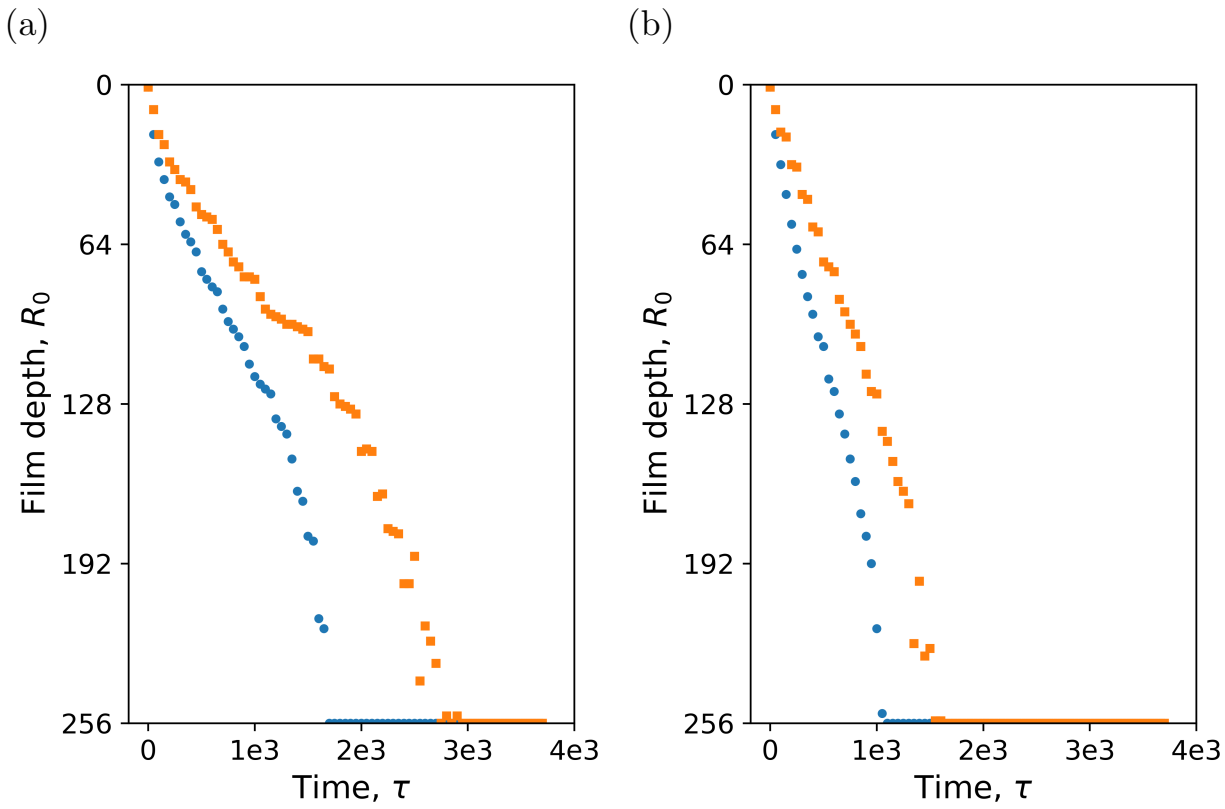

Figure S8: Propagation dynamics of the phase-separation (blue circles) and glass-transition (orange squares) fronts into the film for the 3D NIPS simulations shown in (a) Figure 5 and (b) Figure 6.

Phase separation with hydrodynamics

We used a multi-component diffusion model in our treatment of NIPS for this study, ignoring the role of hydrodynamics. In the solution of the Stokes equation, velocities are scaled by the inverse of mixture viscosity. Due to the high viscosity contrast ($\eta_p/\eta_s = 10^4$) applied for our structural arrest mechanism, we assume that flows in any continuous polymer-rich phase are negligible, allowing phase separation to proceed only by diffusion. The difference between the microstructures of Figures S9a and S9b illustrates the effects of interfacially driven flows on phase separation. In contrast, the microstructures in Figures S10a and S10b are qualitatively the same, owing to the shutdown of the velocities in the presence of glassy dynamics.

Of course, hydrodynamics can prove to be more significant for membrane processes operating in regimes where the continuous polymer-rich phase is not subject to early vitrification. We leave this and other complexities to future study.

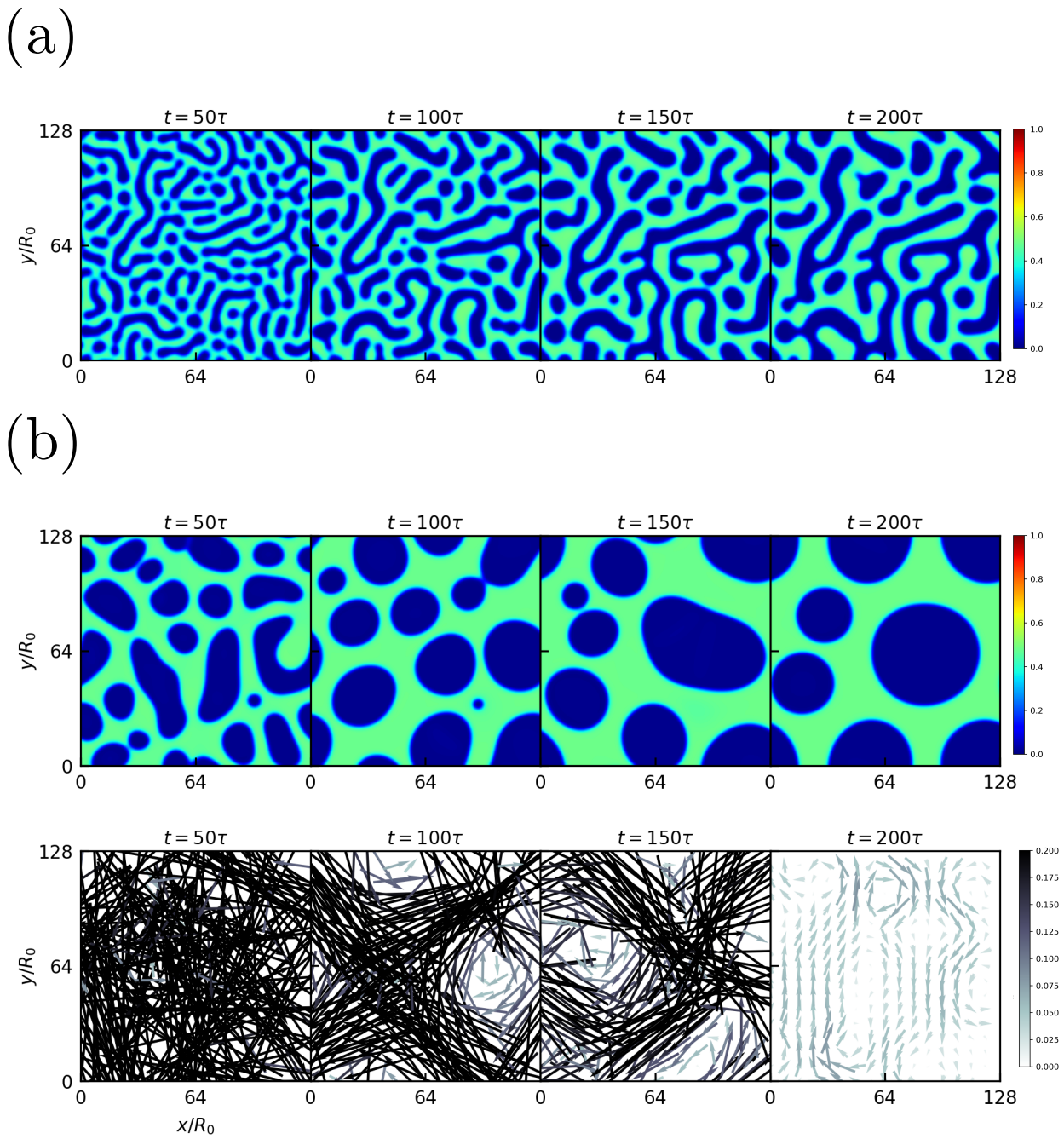

Figure S9: Bulk phase separation dynamics without a glass transition ($\eta_p/\eta_s = 1$), (a) without and (b) with hydrodynamics. The bulk composition was initialized within the spinodal at $\{\phi_p = 0.24, \phi_n = 0.56\}$. In the density fields, polymer-rich is light green and polymer-poor is dark blue. In the velocity fields (bottom panel), darker vectors correspond to higher magnitudes.

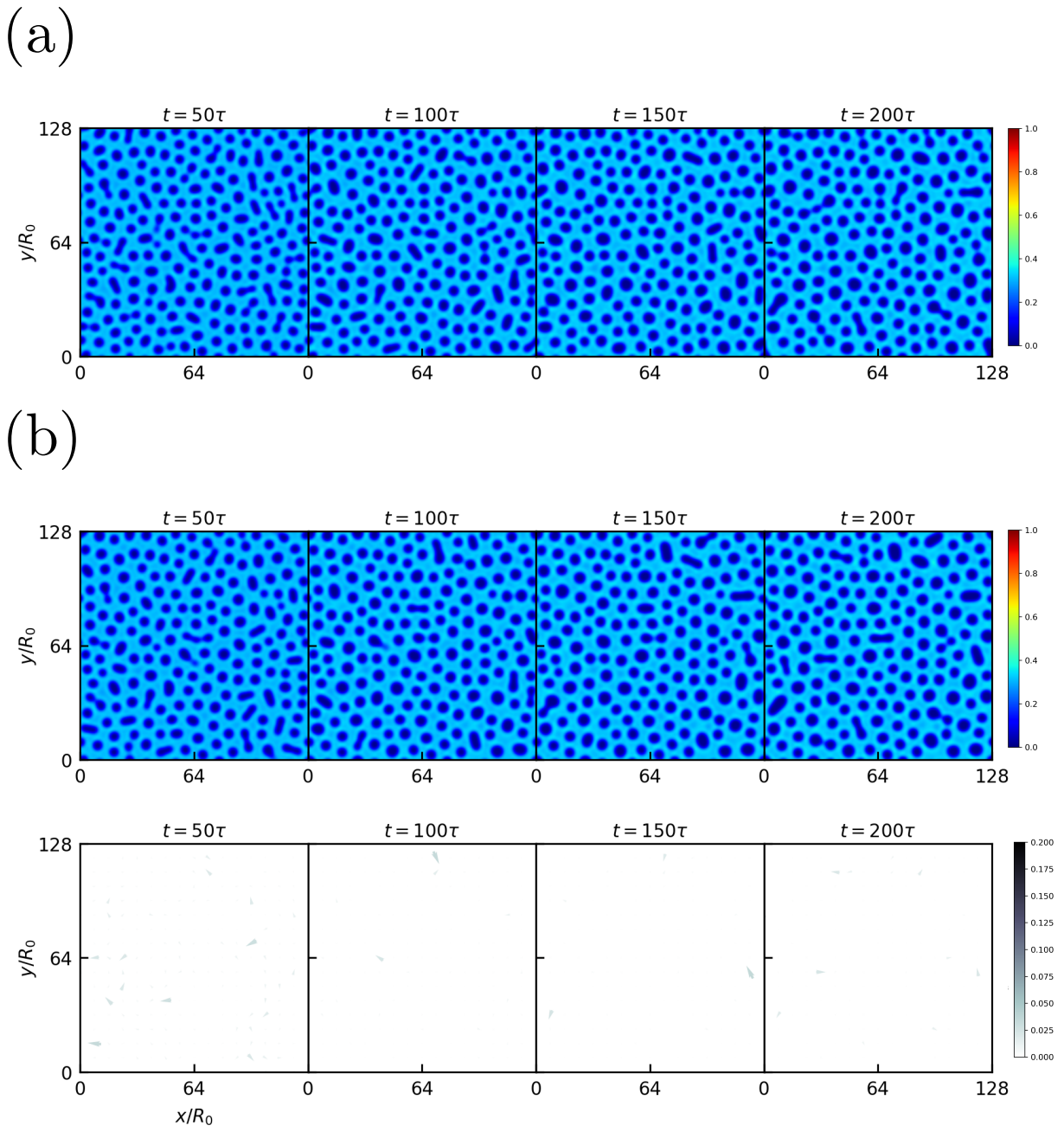

Figure S10: Bulk phase separation dynamics with a glass transition ($\eta_p/\eta_s = 10^4$), (a) without and (b) with hydrodynamics. The bulk composition was initialized within the spinodal at $\{\phi_p = 0.24, \phi_n = 0.56\}$ and the glass-transition concentration set at $\phi_p^* = 0.33$. In the density fields, polymer-rich is light blue and polymer-poor is dark blue. In the velocity fields (bottom panel), darker vectors correspond to higher magnitudes. The same velocity colorbar in Figure S9 was used to illustrate the effect of the viscosity contrast to the magnitude of velocities.

References

(S1) Tree, D. R.; Delaney, K. T.; Ceniceros, H. D.; Iwama, T.; Fredrickson, G. H. A multi-fluid model for microstructure formation in polymer membranes. *Soft Matter* **2017**, *13*, 3013–3030, DOI: 10.1039/C6SM02839J.

(S2) Doi, M.; Onuki, A. Dynamic coupling between stress and composition in polymer solutions and blends. *J. Phys. II France* **1992**, *2*, 1631–1656.

(S3) Hohenberg, P. C.; Halperin, B. I. Theory of dynamic critical phenomena. *Reviews of Modern Physics* **1977**, *49*, 435–479, DOI: 10.1103/RevModPhys.49.435.

(S4) Shimizu, R.; Tanaka, H. A novel coarsening mechanism of droplet spinodal decomposition. *Nature Communications* **2015**, *6*, 1–11, DOI: 10.1063/1.4794613.

(S5) Hiemenz, P. C.; Lodge, T. P. *Polymer Chemistry*, 2nd ed.; CRC Press: Boca Raton, 2007; pp 1–575.

(S6) Zeman, L.; Fraser, T. Formation of air-cast cellulose acetate membranes. Part I. Study of macrovoid formation. *Journal of Membrane Science* **1993**, *84*, 93–106, DOI: 10.1016/0376-7388(93)85053-Y.

(S7) Zeman, L.; Fraser, T. Formation of air-cast cellulose acetate membranes Part II. Kinetics of demixing and microvoid growth. *Journal of Membrane Science* **1994**, *87*, 267–279, DOI: 10.1016/0376-7388(94)87033-0.